Chemical Engineering Journal 533 (2026) 174639

Contents lists available at ScienceDirect

Chemical Engineering Journal

journal homepage: www.elsevier.com/locate/cej

Mechanoadaptive conductive hydrogels with dual functionalities for epidermal sEMG monitoring and diabetic wound healing

Guoqiang Ren [a,d,1], Jingyun Ma [a,1], Qiuyue Peng [c,1], Pengfei Liu [a], Xiaobo Wang [a], Da Li [a], Yuesheng Zhang [d], Chaonan He [a], Chen Huang [e], Honghua Ye [a], Yavuz Nuri Ertas [f,g,*], Qingbo Xu [d,**], Jiangfang Lian [a,**], Mingming Hao [a,b,***]

[a] The Affiliated Lihuili Hospital of Ningbo University, Ningbo, Zhejiang, 315046, China
[b] Suzhou Institute of Nano-Tech & Nano-Bionics (SINANO), Chinese Academy of Sciences (CAS), Suzhou, 215123, China
[c] Department of Health Science and Technology, Aalborg University, Gistrup, 9260, Denmark
[d] Department of Cardiology, The First Affiliated Hospital, Zhejiang University School of Medicine, Hangzhou, Zhejiang, 310003, China
[e] Department of Cell Biology and Genetics, School of Basic Medical Sciences, Xi'an Jiaotong University, Xi'an, Shanxi, 710000, China
[f] Department of Biomedical Engineering, Erciyes University, Kayseri, 38039, Türkiye
[g] Mini-invasive Interventional Therapy Center, Shanghai East Hospital, Tongji University, Shanghai, China

ARTICLE INFO

Keywords:
Conductive hydrogel
Mechanoadaptive hydrogel
Diabetic wound healing
Bioelectronic
Epidermal sEMG monitoring

ABSTRACT

Chronic wounds of diabetes present critical challenges with impaired healing, high infection risk, and poor compatibility of conventional dressings. Effective management requires dressings integrating tissue-matched mechanics, antioxidative/anti-inflammatory activity, and bioelectronic functionalities. Herein, we report a mechanoadaptive and conductive hydrogel (denoted as GPGQ) composed of gelatin, polyvinyl alcohol (PVA), grape seed extract (GSE), and quaternary ammonium chitosan (QAC). GPGQ exhibits state-dependent mechanoadaptability via enhanced hydrogen bonding: in the hydrated state, it shows a tensile strength of 0.10 MPa and compressive strength of 0.20 MPa (matching soft tissue mechanics); upon dehydration, strengths increase to 0.25 MPa and 2.3 MPa (resisting external pressure); rehydration restores >90% flexibility, ensuring long-term adaptability to tissue microenvironments. Its adhesion to porcine skin reaches 60 kPa, facilitating stable contact between the dressing and tissue. GPGQ's 3D porous network (20–80 μm) facilitates cell integration, electrolyte transport, and low-impedance conduction. Electrochemical impedance confirms low skin-electrode impedance ($<10^3$ Ω, 0.1 Hz–100 kHz), while signal tests validate stable sEMG acquisition and resolve 0–300 Hz bands. Biologically, GPGQ promotes fibroblast migration, angiogenesis, and collagen deposition. Grape seed proanthocyanidins suppress IL-1β, IL-6, and TNF-α, elevate IL-10 and TGF-β, and scavenge DPPH radicals and reactive oxygen species (ROS), while stabilizing the glutathione (GSH)/glutathione disulfide (GSSG) ratio. In vivo studies demonstrate that GPGQ accelerates diabetic wound closure through synergistic mechanical support and biochemical modulation. These findings suggest that GPGQ holds promise as a multifunctional dressing for managing chronic wounds associated with diabetes, integrating mechanical adaptability, bioelectronic compatibility, and pro-healing bioactivity.

1. Introduction

Diabetic chronic wounds affect 15–25% of diabetic patients globally, presenting a recalcitrant clinical challenge characterized by impaired healing, heightened infection risk, and poor compatibility with conventional dressings [1–3]. Driven by hyperglycemic conditions, their pathogenesis involves interconnected cascades: elevated ROS disrupt cellular functions, impairing fibroblast activity, angiogenesis, and collagen deposition [4]; prolonged inflammation, sustained by pro-inflammatory cytokines (e.g., IL-1β, IL-6, TNF-α), stalls healing phase

* Correspondence to: Y. N. Ertas, Department of Biomedical Engineering, Erciyes University, Kayseri, 38039, Türkiye.
** Corresponding authors.
*** Correspondence to: M. Hao, [a]The Affiliated Lihuili Hospital of Ningbo University, Ningbo, Zhejiang, 315046, China.
E-mail addresses: yavuznuri@gmail.com (Y.N. Ertas), qingbo_xu@zju.edu.cn (Q. Xu), hjmpin@163.com (J. Lian), 18306213728@163.com (M. Hao).
[1] These authors contributed equally.

https://doi.org/10.1016/j.cej.2026.174639
Received 5 October 2025; Received in revised form 6 February 2026; Accepted 24 February 2026
Available online 25 February 2026

transitions [5]; and compromised immunity fosters bacterial colonization, exacerbating tissue necrosis and delaying re-epithelialization [6]. These pathologies often lead to extensive skin defects, imposing severe physical, psychological, and socioeconomic burdens [7]. Current therapies remain inadequate: glycemic control, debridement, and standard dressings (e.g., hydrocolloids) fail to address multifactorial healing impairments [8]; advanced interventions (growth factors, negative pressure therapy) suffer from high recurrence rates, inconsistent efficacy, and lack of dynamic monitoring [9,10]; and conventional dressings exhibit mechanical mismatch with soft tissues and insufficient bioactive modulation [11].

Hydrogels have emerged as transformative candidates for chronic wound management, owing to their tissue-mimetic hydration, biocompatibility, and modular functionality [12,13]. Their three-dimensional hydrated network promotes tissue regeneration, while tunable mechanical properties ensure intimate conformation to irregular wound surfaces, effectively reducing mechanical stress and enhancing healing efficiency [14,15]. Among these, conductive hydrogels have garnered significant attention, as they integrate electrical conductivity with bioactivity, enabling dual functionalities: electrical signals guide cell migration (electrotaxis) and enhance angiogenesis [16,17], while conductive properties support real-time bioelectronic monitoring (e.g., impedance, electromyography) to assess healing dynamics [18,19]. The necessity for such bioelectronic monitoring stems from the limitations of traditional wound assessment, which relies on subjective visual inspection and fails to identify underlying healing barriers early. Impedance spectroscopy can directly reflect tissue microenvironments—e.g., persistent low impedance suggests edema, stalled inflammation, or infection—while sEMG captures neuromuscular signals to indirectly assess blood supply and reinnervation. Integrating these methods allows for dynamic, objective tracking of the entire healing process, providing a critical basis for timely intervention [20]. For instance, conductive hydrogels loaded with antimicrobial agents or growth factors have shown promise in accelerating wound closure [21,22], while those incorporating conductive polymers (e.g., polypyrrole, graphene derivatives) have demonstrated potential for electrophysiological signal acquisition [23,24].

However, critical limitations persist in existing conductive hydrogels. Mechanical mismatch remains a key barrier: overly soft formulations lack structural integrity to resist external pressure, while rigid ones induce tissue stress and detachment [18,25]. Additionally, many lack robust antioxidant/anti-inflammatory activity to counteract ROS and chronic inflammation in diabetic wounds [26]. Poor interfacial adhesion and high electrical impedance further compromise stable signal acquisition, limiting their utility in continuous bioelectronic monitoring [27]. Thus, there is an urgent need for a multifunctional hydrogel platform that integrates state-dependent mechanical adaptability (matching soft tissue in hydration, resisting pressure upon dehydration), low-impedance conductivity for high-fidelity signal acquisition, potent bioactivity (antioxidant, anti-inflammatory, pro-healing), and robust tissue adhesion capabilities critical for addressing the complex demands of diabetes-associated chronic wound management.

Herein, we report a GPGQ mechanoadaptive conductive hydrogel that exhibits state-dependent mechanical adaptability: enhanced hydrogen bonding enables hydrated properties that match soft tissue mechanics, while dehydrated properties resist external pressure, making it restorable upon rehydration. Its 3D porous network facilitates electrolyte transport, while low electrochemical impedance enables high-fidelity sEMG acquisition. Biologically, GPGQ leverages GSE proanthocyanidins to scavenge ROS, modulate inflammatory cytokines, and promote fibroblast migration, angiogenesis, and collagen deposition. In vivo studies confirm its ability to accelerate diabetic wound closure via synergistic mechanical support and biochemical modulation. This work demonstrates that GPGQ holds promise as a multifunctional dressing, bridging mechanical adaptability, bioelectronic compatibility, and pro-healing bioactivity for integrated diabetes-associated chronic wound management (Scheme 1A).

2. Experimental section

2.1. Preparation of the hydrogel

Solution A (20 *w/v*% PVA) was prepared by dissolving 40 g PVA (PVA-117, molecular weight ~ 145,000, Shanghai Aladdin Industrial Corporation Co. Ltd) in 160 mL deionized water at 90 °C for 6 h, while solution B (10 w/v% gelatin) was made by dissolving 20 g gelatin (Glue strength ~100 g Bloom, Shanghai Aladdin Industrial Corporation Co. Ltd) in 180 mL deionized water at 60 °C for 6 h. Equal volumes (50 mL) of both solutions were then mixed and stirred at 60 °C to form the PG solution. For the PGQ solution, 49 mL of solution A was mixed with 2 g of QAC (Degree of substitution, 40%; Shanghai Maclin Biochemical Technology Co., Ltd.) before being combined with 49 mL of solution B. For the GPGQ solution, 48.5 mL of solution A was mixed with 2 g of QAC and 1 g of GSE (Purity ≥95%, Shanghai Aladdin Industrial Corporation Co., Ltd.) before adding 48.5 mL of solution B. All solutions were degassed via ultrasonic treatment, cast into molds, and subjected to three freeze-thaw cycles (−80 °C for 6 h followed by natural thawing for 12 h).

2.2. Characterization of the physical and chemical properties

Micro-CT and SEM observations: The microarchitecture, pore structure, and pore size distribution of the hydrogels, before and after dehydration, were analyzed using a high-resolution Micro-CT system (VENUS® Micro CT, Ping Sheng Medical Technology, Kunshan, China) and a scanning electron microscope (SEM) (SU8010, Hitachi, Germany). Hydrogel samples were cut into thin sections (5 mm diameter, 1 mm thick) and snap-frozen at −80 °C for 2 h. They were then freeze-dried at −55 °C for 12 h under 0.22 atm. After drying, the samples were sealed in glass vials containing calcium chloride desiccant. Before SEM imaging, the samples were sputter-coated with a thin gold layer to improve conductivity. The pore size distribution was determined by combining SEM and micro-CT analyses. For SEM, pore equivalent spherical diameters were measured from five non-overlapping cross-sectional areas per sample using ImageJ's "Analyze Particles" function, with ≥100 pores per sample analyzed. Micro-CT validated these results through 3D reconstruction and threshold segmentation of a 1 mm^3 hydrogel volume. Data represent means from three independent replicates.

Adhesion strength test: The adhesion strength of the hydrogel was tested by attaching hydrogel film strips (100 × 20 × 2 mm) to fresh porcine skin rectangles (200 × 40 × 2 mm), with an adhesive area of 70 × 20 mm and a 10 mm gap. Adhesive strength was measured at 25 ± 2 °C and 50 ± 5% humidity using a Universal Testing Machine (Instron 3365, USA) at a loading rate of 5 mm/min.

Mechanical properties test: The mechanical performance of the hydrogels was systematically evaluated under both tensile and compressive loading conditions. For tensile testing, hydrogel films (50 × 20 × 2 mm) were measured using a universal testing machine with an initial gauge length of 20 mm and a crosshead speed of 10 mm/min. The tensile modulus was calculated from the slope of the stress–strain curve at 10% strain. For compressive testing, cylindrical specimens (20 mm in diameter and 10 mm in height) were tested with an initial gap of 15 mm and a loading rate of 2 mm/min. The compressive modulus was determined from the slope of the stress–strain curve at 20% strain. All tests were conducted in ambient air at 25 ± 2 °C and 50 ± 5% relative humidity. To evaluate the mechanical recovery under cyclic loading, compression tests were further conducted on hydrogels in three hydration states. Cylindrical specimens (Φ10 × 5 mm) underwent five consecutive compression cycles at a strain of 30% and a strain rate of 10 mm/min, with 30-s recovery intervals between cycles.

Relaxation and creep tests: GPGQ hydrogels were subjected to stress relaxation and creep tests using a Universal Testing Machine. Tensile

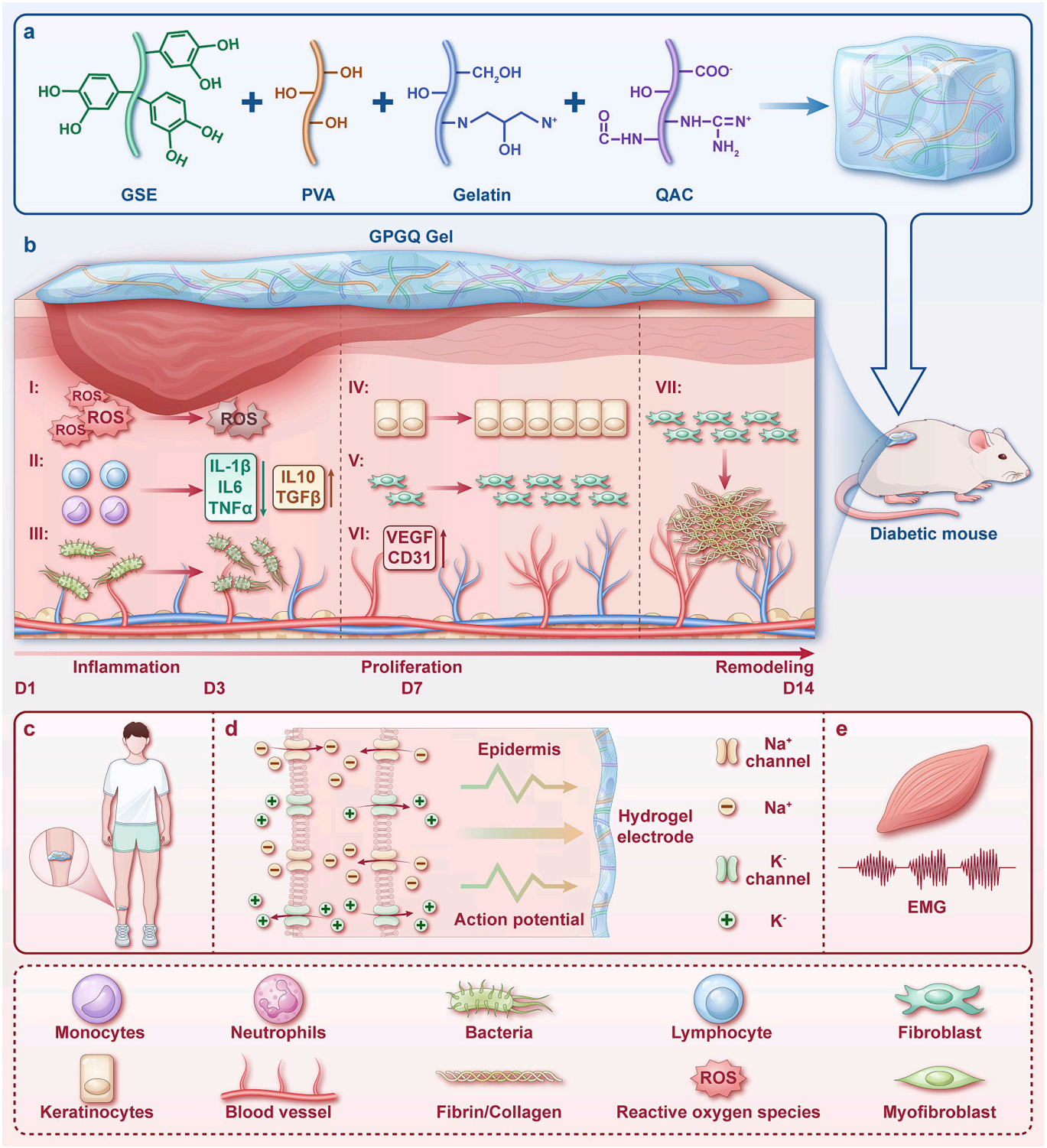

Scheme 1. Mechanoadaptive conductive hydrogels for diabetic wound healing and epidermal sEMG monitoring. a) Preparation of GPGQ hydrogels: GSE, PVA, gelatin, and QAC form a network via enhanced hydrogen bonding. b) Wound-healing mechanism of GPGQ: Proanthocyanidins in GSE scavenge ROS, regulate cytokines (inhibit IL-1β/IL-6/TNF-α, elevate IL-10/TGF-β), stabilize redox balance (GSH/GSSG), and boost re-epithelialization. GPGQ also promotes fibroblast migration, angiogenesis, and collagen deposition, modulating signaling to accelerate repair. c-e), GPGQ, being soft, skin-conformal, and ionically conductive, acts as an on-skin electrode for sEMG monitoring, detecting action potentials via ion transport to sense muscle activity.

tests were conducted at a strain rate of 10 mm/min, with stress relaxation measured under 10% incremental strain (10%–60%) for 2000 s. Creep tests were performed under a constant stress of 0.1 MPa on cylindrical samples (20 mm diameter, 10 mm thickness), with deformation recorded at 10 ms intervals for 10 h using a laser displacement sensor (Keyence, LK-H052).

Electrical performance test: All electrochemical measurements were carried out at room temperature using a CHI660E electrochemical workstation (CH Instruments, Shanghai, China) in a three-electrode configuration. An Ag/AgCl electrode served as the reference electrode,

a platinum wire as the counter electrode, and the hydrogel sample as the working electrode, with an effective area of 1 cm^2. The testing medium was a 0.9 *w/v*% NaCl physiological saline solution to simulate the biological environment. Electrochemical impedance spectroscopy (EIS) was performed over a frequency range of 0.01 Hz to 100 kHz with an AC amplitude of 10 mV to evaluate the ionic conductivity and interfacial impedance characteristics of the hydrogel. To further investigate the hydrogel's electrical signal transmission capability, square and sine waveforms (0.1–100 kHz) were generated using a function generator (AFG2021, Tektronix, USA) and passed through the hydrogel. The transmitted signals were recorded in real-time using a digital oscilloscope (DPO5034B, Tektronix, USA) to assess waveform fidelity and frequency response.

sEMG signal monitoring: sEMG signals were recorded using a Sessantaquattro+ system (OT Bioelettronica S.r.l., Italy). The recording electrodes consisted of a flexible 8-channel substrate with exposed circular gold electrode sites (3 mm in diameter). For signal acquisition, a GPGQ hydrogel pad (5 mm in diameter, 0.5 mm thick) was placed on each electrode site to ensure conformal coverage and enhanced electrode–skin contact. To improve visual contrast during placement, the hydrogel was colored with edible blue dye. The test subject was the corresponding author (Mingming Hao). The study protocol was approved by the Affiliated Lihuili Hospital of Ningbo University (KY2023SL036–02) and Ningbo University (12312) and was conducted in accordance with the Declaration of Helsinki. Ethics approval and informed consent were obtained from all participants.

2.3. Evaluation of cytocompatibility, hemocompatibility, and histocompatibility

Hydrogel extract was prepared by soaking 0.1 g of hydrogel in 10 mL of culture medium for 24 h. Human dermal fibroblasts (HDFs, Procell, Wuhan, China) at 5×10^4 cells per well in 6-well plates were exposed to the extract for 1 or 3 days, then stained with the LIVE/DEAD Cell Imaging Kit (R37601, Invitrogen) and examined under a fluorescence microscope. Live cells (green fluorescence) and dead cells (red fluorescence) were counted, and cell viability was calculated as the ratio of live cells to total cells. After 1 or 3 days of culture with the extract, cells were incubated with CCK-8 reagent (Beyotime Biotechnology, Shanghai, China) for 1 h, and absorbance was measured at 450 nm. For the hemolysis assay, fresh mouse blood cells were diluted to 5% (*w/v*), and 0.1 g of hydrogel was incubated with 10 mL of the suspension at 37 °C for 1 h. Deionized water was used as the positive control to induce 100% hemolysis, and PBS was used as the negative control with 0% hemolysis. The absorbance of the supernatant was measured at 540 nm. The hemolysis rate was calculated as (ODn-ODc) / (ODs-ODc) × 100%, where ODn, ODc, and ODs represent the absorbance from hydrogel, PBS, and deionized water, respectively. For in vivo histocompatibility testing, major organs (heart, liver, spleen, lungs, and kidneys) were collected from 6-week-old BALB/c mice 40 days after treatment, fixed, and stained with H&E. A sham-operated control and a hydrogel-implanted group with subcutaneous dorsal injection were used. Tissue sections were microscopically examined for inflammation, necrosis, and organ damage.

2.4. Antioxidant and antibacterial effects

Antioxidant activity was evaluated using the DPPH assay, where hydrogel extract (equivalent to 10 mg hydrogel per mL culture medium) was mixed with a 200 mM DPPH solution (in methanol) at a 1:1 volume ratio, incubated for 30 min, and the optical density was measured at 517 nm. For the ROS assay, L929 cells were exposed to the hydrogel extract and hydrogen peroxide (H_2O_2, 3 μg/mL) for 4 h, followed by incubation with DCFH-DA probe (10 μM) for 30 min in the dark, and then fluorescence images were acquired. In addition, L929 cells (Procell) at 3×10^3 after exposure were lysed to extract proteins for measuring superoxide dismutase (SOD), malondialdehyde (MDA), and the GSH/GSSG ratio, according to the manufacturer's instructions (S0101S, S0131S, and S0053, Beyotime Biotechnology). For antibacterial evaluation, sterile hydrogel discs (diameter 10 mm, thickness 2 mm) of GPGQ, PGQ, and PG were placed onto agar plates pre-inoculated with 100 μL of either *Escherichia coli* (*E. coli*, a gram-negative bacterium) or *Staphylococcus aureus* (*S. aureus*, a gram-positive bacterium) suspension (1×10^7 CFU/mL). All plates were incubated at 37 °C for 24 h. The diameter of the inhibition zone was measured in millimeters at three perpendicular directions, and the average value was calculated. To quantitatively assess antibacterial efficacy, the minimum inhibitory concentration (MIC) of hydrogel extracts was determined. Serial two-fold dilutions of the extracts, ranging from 0.5 to 10 mg/mL equivalent hydrogel concentration, were prepared and inoculated with bacterial suspensions at approximately 5×10^5 CFU/mL. The inoculated samples were incubated at 37 °C for 18 h. Bacterial growth was monitored by measuring the optical density at 600 nm (OD600) using a microplate reader. To correct for background absorbance, the OD600 values of corresponding blank controls (culture medium without bacteria) were subtracted from each measurement. The MIC was defined as the lowest hydrogel extract concentration at which the background-corrected OD600 was $\leq$0.05, indicating complete inhibition of bacterial growth.

2.5. Scratch assay and tube formation assay

The scratch wound healing assay was performed using confluent HDFs cultured in 6-well plates at a density of 5×10^5 cells per well. After 12 h of serum starvation, uniform scratches were created using 200 μL pipette tips. After scratching, the wells were gently washed with PBS to remove detached cells, and then the hydrogel extract was added. Test groups received hydrogel extract (10 mg/mL in 1% FBS medium) while control groups received 1% FBS medium alone. Scratch closure was monitored by phase-contrast microscopy at 0, 12, 24, and 36-h timepoints. Wound healing rates were quantified using ImageJ by calculating the percentage of wound closure relative to the initial scratch area. For the tube formation assay, 50 μL of Matrigel (Corning, 356234) was plated per well in 96-well plates and polymerized at 37 °C for 30 min. HUVECs (Procell) were seeded at 2×10^4 cells/well in hydrogel extract (10 mg/mL) with 1% FBS and incubated for 12 h. Tube structures were imaged under a microscope, and angiogenesis parameters (total tube length, number of junctions, and number of tubes) were quantified using ImageJ.

2.6. Animal experiments on wound healing

All experimental protocols involving animals were approved by the Animal Care and Use Committee of Ningbo University, under the Approval No. 12644. After a 10-h fast, 6-week-old male C57BL/6 mice received STZ solution (50 mg/kg, 50 mg/mL in 0.1 M citrate buffer, pH 4.5) via intraperitoneal injection for three consecutive days. One week later, mice with blood glucose levels exceeding 16.7 mmol/L were selected to establish a type 1 diabetes model. Full-thickness dorsal wounds (0.8 cm diameter) were created on each mouse using a sterile biopsy punch, and bleeding was stopped by gentle pressure with sterile gauze, which was then randomized into four groups ($n = 6$). The hydrogel was meticulously cut into 1 cm diameter circles prior to use. The wounds were treated three times with either the test hydrogel (GPGQ hydrogel, PGQ hydrogel, and PG hydrogel) or 3 M Tegaderm (standard wound dressing control) on days 0, 3, and 7, with thorough documentation of the wound area on days 0, 3, 7, 10, and 14. The wound area was calculated using ImageJ software based on digital photographs. To prevent hydrogel displacement and wound contraction, a semi-permeable barrier dressing and an elastic bandage were applied to the wound site in all groups. Wound tissue samples were collected on days 3 and 14 and fixed in 4% paraformaldehyde for histological analysis (H&E and Masson trichrome staining) and immunohistochemistry to assess

key inflammatory (IL-1β, IL-6, TNF-α, IL-10, TGF-β) and healing markers (CD31, VEGF, PCNA). Protein levels of inflammatory (IL-1β, IL-6, TNF-α, IL-10, TGF-β) and angiogenic factors (VEGF) in wound tissue homogenates were measured via ELISA on day 3. ELISA kits (R&D Systems, cat. no. MLB00C-1 for IL-1β; Abcam, cat. no. ab222503 for IL-6; R&D Systems, cat. no. MTA00B-1 for TNF-α; Abcam, cat. no. ab108870 for IL-10; Abcam, cat. no. ab119557 for TGF-β; Abcam, cat. no. ab209882 for VEGF) were used according to the manufacturers' instructions.

2.7. Statistical analysis

Statistical analyses were performed on independent biological replicates (animals or wells), with sample sizes (n) indicated in figure legends. Data are presented as mean ± 95% confidence interval (CI). Randomization and blinding were applied where feasible to minimize experimental bias. Normality and homogeneity of variance were tested prior to analysis. Parametric comparisons were conducted using one-way ANOVA followed by Tukey's post-hoc test; otherwise, Kruskal–Wallis with Dunn's multiple comparisons test was used. Statistical significance is denoted as $*p < 0.05$, $**p < 0.01$, $***p < 0.005$ and $****p < 0.0001$.

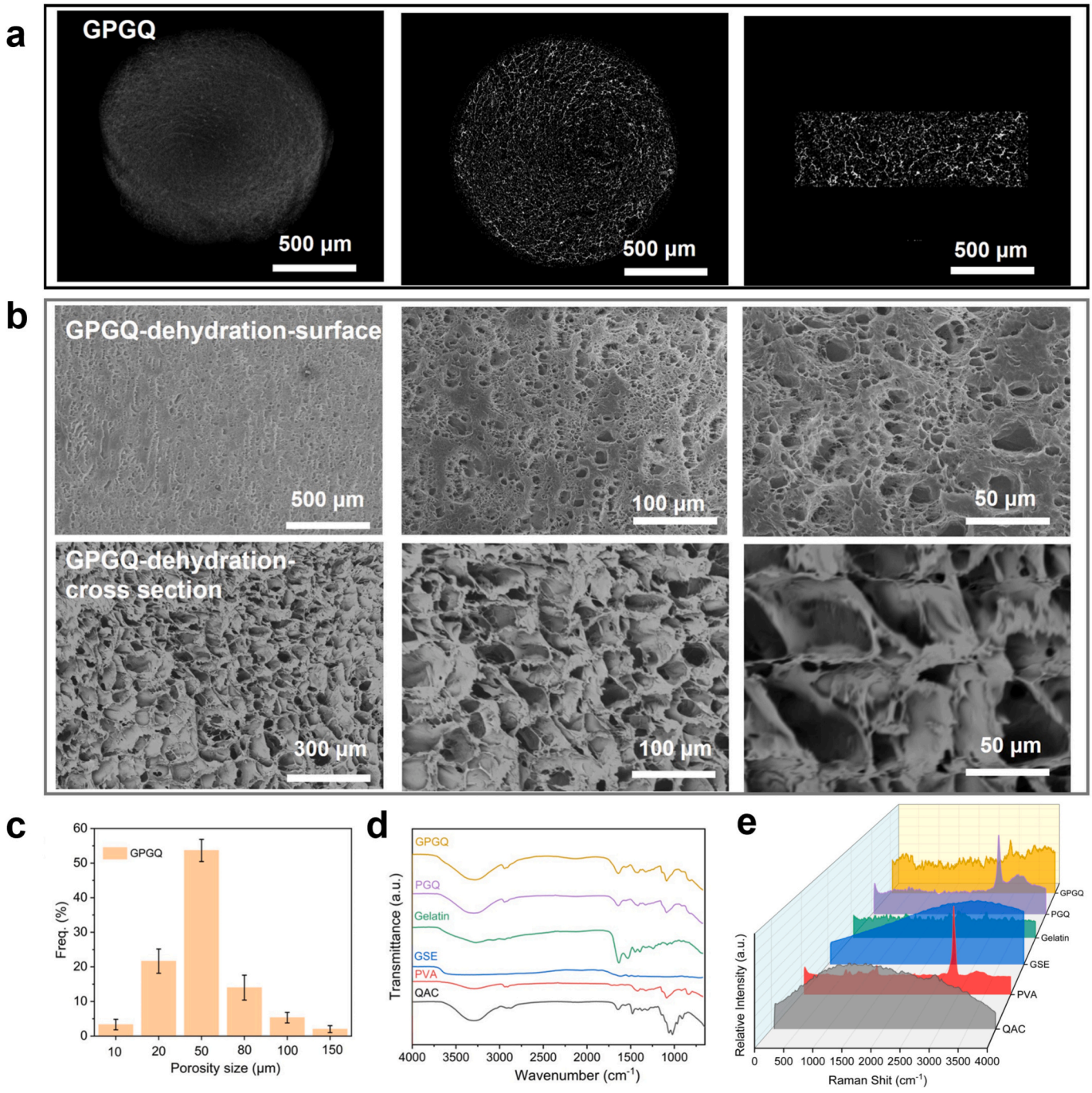

Fig. 1. Microstructural and spectroscopic characterization of the GPGQ hydrogel. a) Micro-CT reconstruction images. b) SEM images at various magnifications. c) Pore size distribution histogram. d) FTIR spectra of GPGQ and its individual constituents. e) Raman spectra of GPGQ and its individual constituents.

3. Results and discussion

3.1. Microstructural and spectroscopic characterization of GPGQ hydrogel

The microstructure of hydrogels plays a critical role in wound healing. Hydrogels with pore sizes ranging from tens to hundreds of micrometers, combined with high porosity and interconnectivity, facilitate cell attachment and migration, thereby promoting tissue repair [28]. Additionally, an open, porous structure improves drug-loading capacity, while tailored pore architectures enable controlled release kinetics. Furthermore, mechanics tuned through microstructure design can better match native tissues, minimizing irritation and enhancing biocompatibility [14]. The microstructure and molecular interactions of several hydrogels were systematically evaluated using a multi-technique approach, including micro-computed tomography (Micro-CT), scanning electron microscopy (SEM), and spectroscopic analysis.

Fig. 1a presents representative Micro-CT graphs of the GPGQ material. The images reveal a highly porous architecture, characterized by irregularly shaped, interconnected pores that form a continuous network throughout the structure. The consistent morphological features observed across all panels (oblique, surface, and cross-sectional view) indicate a porous organization within the material. Fig. 1b shows that the GPGQ hydrogel exhibits a continuous, interconnected porous structure both on the surface and in cross-section. Although surface pore sizes (average ~ 20 μm) are slightly smaller than those in cross-sections (average ~ 50 μm), both are predominantly distributed within the 20–80 μm range. The cross-sectional view reveals elongated, non-equiaxed pores, suggesting a potentially aligned and anisotropic network. This morphological feature is consistent with unidirectional ice crystal growth during the freeze-thaw process. The overall network exhibits no significant collapse or discontinuities, demonstrating excellent pore connectivity. This structure facilitates cell migration and electrolyte transport, meeting the microstructural requirements for wound healing and electrophysiological signal monitoring [29]. The combination of overall porosity and guided microchannels indicates a strong suitability for advanced tissue engineering applications [30]. As shown in Fig. 1c, the pore sizes of the GPGQ hydrogel predominantly ranged from 20 to 80 μm, with a pronounced peak at 50 μm, accounting for 55% of all pores. For comparison, we also characterized the microstructures and pore-size distributions of the intermediate PG and PGQ hydrogels obtained during GPGQ synthesis. As shown in Fig. S1, both PG and PGQ hydrogels exhibited less-integrated pore architectures than GPGQ. This divergence originates from fundamental differences in their cross-linking networks. Quantitatively, the pore size of PG hydrogels was predominantly distributed within the 100–300 μm range, with a peak at 200 μm, accounting for approximately 75% of the total pores. The broad distribution and structural instability arise from the relatively weak and transient nature of the physical cross-linking between PVA and gelatin, primarily through hydrogen bonding. This network lacks sufficient robustness to fully withstand the capillary forces and polymer chain rearrangement during freeze-drying, leading to partial pore collapse and compromised interconnectivity. PGQ hydrogels exhibited a narrower pore-size distribution, centered at 80 ± 20 μm, indicating a more consolidated structure due to QAC incorporation. The quaternary ammonium groups on QAC introduce additional electrostatic interactions and potential ionic cross-linking, enhancing the network's cohesion and yielding a more uniform pore structure. However, the PGQ network still lacks the synergistic, multi-point reinforcement found in GPGQ. The proanthocyanidins from GSE act as multi-functional cross-linkers, capable of forming extensive hydrogen bonds simultaneously with hydroxyl groups on PVA, amino groups on gelatin, and quaternary ammonium groups on QAC. This creates a denser, more resilient, and more integrated network in GPGQ, which better maintains its architectural integrity during processing and explains its superior pore-structure uniformity and interconnectivity, as observed in Fig. 1b and Fig. S1.

Fig. 1d presents the Fourier-transform infrared (FTIR) spectroscopy analysis of the GPGQ composite hydrogel alongside its individual constituents (gelatin, PVA, QAC, and GSE). The GPGQ spectrum incorporates characteristic absorption bands from each component, including broad –OH/–NH stretching vibrations around 3300–3400 cm^{-1}, a carbonyl stretching peak near 1650 cm^{-1}, and C–O–C/C–N vibrations between 1000 and 1100 cm^{-1}. Critically, the FTIR profile of GPGQ does not correspond to a simple superposition of the individual spectra, suggesting the emergence of new intermolecular interactions—such as hydrogen bonding and van der Waals forces—during hydrogel formation. These interactions contribute to a stable cross-linked network, enhancing both mechanical integrity and electrical performance [31]. Raman spectroscopy (Fig. 1e) further corroborates the molecular structure of GPGQ, showing prominent peaks at 1350 cm^{-1}, 1580 cm^{-1}, 2900 cm^{-1} (C—H stretching), and 3200–3400 cm^{-1} (O–H/N–H stretching). The observed band shifts and overlap relative to the constituent spectra confirm synergistic molecular reorganization within the composite. The broadening of characteristic peaks—particularly in the FTIR —OH/—NH region (3300–3400 cm^{-1}) and the Raman active modes—arises from enhanced intermolecular interactions among PVA, gelatin, QAC, and GSE, rather than background noise. These interactions facilitate the formation of a densely cross-linked network, which, in conjunction with the interconnected porous microstructure (20–80 μm) observed in Figs. 1b-c, establishes a hierarchical architecture conducive to efficient charge transport. The porous network provides continuous pathways for ion migration, while the molecular-level interactions enhance charge mobility across the polymer matrix. This multi-scale structural design lays the foundation for the hydrogel's performance as a bioelectronic interface material.

3.2. Mechanical characterization of GPGQ hydrogel

Different wound types exhibit distinct biomechanical microenvironments, underscoring the need for hydrogel dressings with tailorable mechanical properties and high tissue compatibility [32]. Since native soft tissues display pronounced viscoelastic behavior—such as stress relaxation and creep—mimicking these characteristics is essential for the design of functional hydrogel dressings. In this context, we conducted a systematic mechanical and rheological characterization of the GPGQ hydrogel.

The basic mechanical properties of a material determine its ability to withstand various stresses during the initial implantation period [33]. Therefore, we first evaluated the core mechanical indicators of the GPGQ hydrogel under static and monotonic loading conditions. Fig. 2a shows that the GPGQ hydrogel exhibits noticeable deformation under both tensile and compressive static loading, demonstrating its flexibility, deformability, and mechanical adaptability. The material can be readily bent, stretched, and pressed, indicating convenient handling and shape adaptability for implantation and tissue conforming. Its stable attachment to skin-like surfaces suggests potential for biomedical applications such as wound dressing and tissue-integrated implants.

In practical applications, hydrogels may experience moisture loss during prolonged wear or exposure to air, and may require rapid rehydration to regain functionality upon exposure to wound exudate or treatment [34]. Therefore, it is essential to evaluate the mechanical performance of the hydrogel across these different hydration states to ensure that it maintains stable adhesion and provides appropriate mechanical support under fluctuating conditions. GPGQ hydrogel samples in native, dehydrated, and rehydrated states demonstrate their reversible hydration-dependent swelling behavior (Fig. S2). Correspondingly, Figs. 2b-d show the ability of GPGQ hydrogels to dynamically regulate their tensile, compressive, and adhesive properties under native, dehydrated, and rehydrated conditions. This adaptability enhances the mechanical stability and environmental adaptability of hydrogels under different wound conditions. The tensile properties of the GPGQ hydrogel

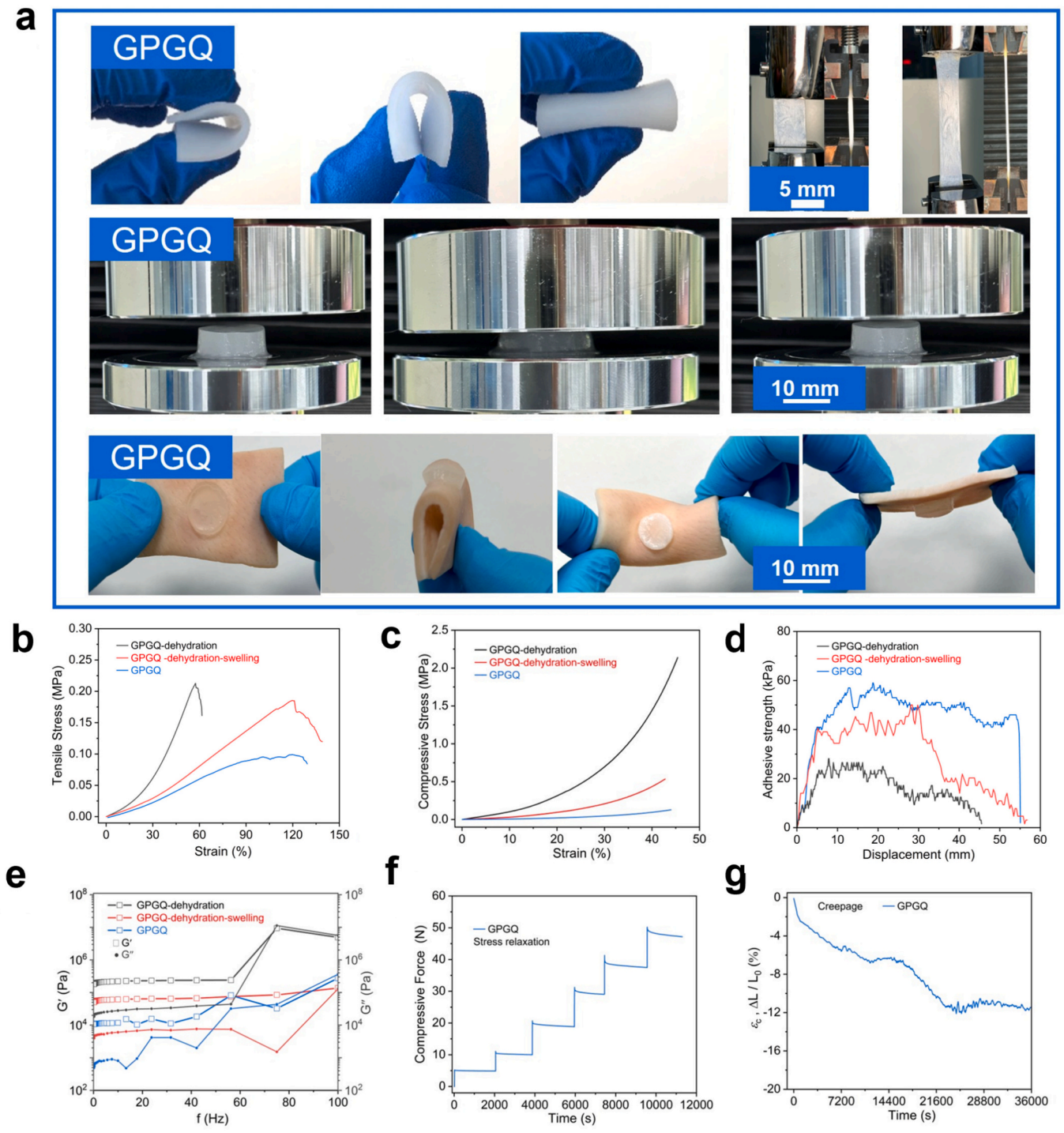

Fig. 2. Mechanical characterization of GPGQ hydrogel. a) Representative optical images of GPGQ hydrogel during tensile, compression, and adhesion tests. b-d) Mechanical quantitative characterization of the tensile, compressive, and adhesive properties of GPGQ hydrogels under different hydration states (original, dehydrated, and rehydrated). e) Rheological properties of hydrogels under different hydration states. f) Stress relaxation behavior of hydrogels. g) Creep performance of hydrogels under constant load.

under different hydration states are summarized in Fig. 2b and Fig. S3a. In its native state, the material exhibited a tensile strength of 0.10 MPa (±0.02), a fracture strain of 130% (±5%), and an elastic modulus of 0.08 MPa (±0.02). After freeze-drying, the tensile strength increased significantly to 0.20 MPa (±0.05), while the fracture strain decreased to 60% (±5) and the modulus rose to 0.35 MPa (±0.05). Following rehydration, the tensile strength remained elevated at 0.18 MPa (±0.02), with partial recovery of flexibility indicated by a fracture strain of 120% (±5) and a reduced modulus of 0.15 MPa (±0.02). The compressive properties of the GPGQ hydrogel across the three hydration states are summarized in Fig. 2c and Fig. S3b. Under 45% strain in the native state, the material exhibited a compressive strength of 0.20 MPa (±0.05) and a modulus of 0.10 MPa (±0.05). After freeze-drying, both properties increased markedly, with compressive strength reaching 2.2 MPa (±0.2) and modulus rising to 3.5 MPa (±0.2). Upon rehydration, the compressive strength decreased to 0.45 MPa (±0.1) and the modulus

reduced to 1.0 MPa (±0.1), reflecting a partial recovery of compressibility. Adhesive strength, a critical indicator of hydrogel dressing efficacy, was evaluated for tissue adherence under different hydration states (Fig. 2d and Fig. S3c). The native GPGQ hydrogel exhibited an adhesion strength of 60 kPa (±5) on porcine skin, significantly higher than that in the dehydrated (25 ± 5 kPa) and rehydrated (45 ± 5 kPa) states. The decline after dehydration is attributed to the loss of hydrophilic groups, reduced chain flexibility, and diminished availability of functional groups for interfacial interaction. Although rehydration partially restored segmental mobility, the irreversible structural reorganization that occurred during freeze-drying impeded the full recovery of adhesion.

The dynamic properties of a material indicate its stability in dynamic environments within the body (such as muscle movement and pulse) [30]. We use the response of materials under alternating loads or shear forces to reflect their viscoelastic nature. Rheological properties of the GPGQ hydrogel under different hydration states are presented in Figs. 2e and Figs. S3d–e. In the native state, the hydrogel showed low storage (G′) and loss (G″) moduli, consistent with a soft, elastic network. A loss factor (tan δ) greater than 1 at high frequencies indicated pronounced viscoelasticity and efficient energy dissipation. The low complex viscosity (|η|) further indicated facile shear deformability. Freeze-drying led to a substantial increase in both G′ and G″, reflecting enhanced crosslinking and structural rigidity. This was accompanied by a decrease in tan δ and an increase in viscosity, indicating greater stiffness and reduced energy dissipation. After rehydration, both moduli decreased but remained elevated relative to the native state, indicating a partial recovery of softness and a persistent strengthening of the hydrogel matrix. The exceptional mechanical stability of GPGQ hydrogel is further demonstrated by cyclic compression tests under three hydration states (hydrated, dehydrated, and dehydro-swollen). As shown in Figs. S3f–h, the hydrogel exhibits highly reproducible stress–strain curves over five consecutive cycles, with minimal residual deformation and full recovery upon rehydration. This reversible, hydration-dependent mechanical behavior originates from a dynamic yet robust cross-linked network that enables effective energy dissipation and structural restoration. Such adaptive performance highlights the potential of GPGQ hydrogel as a smart wound dressing capable of maintaining mechanical integrity across varying moisture conditions during healing.

The time-dependent behavior of materials is critical for their long-term structural and functional integrity, such as resisting creep-induced collapse or avoiding stress failure due to relaxation [19]. We therefore evaluated the long-term stability and suitability of the GPGQ hydrogel as a biomaterial using stress-relaxation tests. As shown in Fig. 2f, under constant strain, the compressive stress of the hydrogel decreased over time and eventually stabilized, demonstrating significant stress relaxation. This viscoelastic behavior stems from its dynamic cross-linked network formed by hydrogen bonding and van der Waals forces among PVA, gelatin, QAC, and GSE. When subjected to constant compressive strain, dynamic bonds (e.g., hydrogen bonds) gradually dissociate, allowing polymer chains to slip and rearrange, thereby progressively releasing internal stress and leading to the observed decay in compressive stress. This stress relaxation capability enables the hydrogel to adapt to skin deformation, effectively reducing localized pressure on wounds or nerve endings, thereby supporting its use in long-term wearable monitoring systems and advanced wound dressings [26]. Creep experiments (Fig. 2g) revealed that under a constant load, the hydrogel underwent gradual deformation yet reached equilibrium without rupture, confirming its buffering capability and dimensional stability. These characteristics are critical for ensuring extended wearability and gentle adaptation to skin movement, thereby promoting minimal motion artifacts and reliable bioelectrical signal acquisition.

The mechanical evaluation of PG, PGQ, and GPGQ hydrogels demonstrated that the incorporation of QAC and subsequent crosslinking significantly enhanced both tensile and compressive properties. As shown in Fig. S4a and S4c, the GPGQ hydrogel exhibits superior tensile and compressive strength compared to PG and PGQ, as directly evidenced by its higher fracture stress in tension and the significantly greater stress it sustains under compression at equivalent strain levels. Furthermore, GPGQ hydrogels also possessed the highest elastic moduli (Fig. S4b, d), indicating substantially improved stiffness and resistance to deformation. These results unequivocally demonstrate the enhanced mechanical robustness of GPGQ and suggest that crosslinking plays a crucial role in reinforcing the hydrogel network, making it a promising candidate for applications that require robust mechanical performance.

The GPGQ hydrogel exhibits versatile mechanical properties, including tensile, compressive, and adhesive properties, across multiple hydration states, which is attributed to its underlying viscoelastic behavior governed by polymer chain slippage, reversible weak bond dissociation, and macromolecular rearrangements. These mechanisms endow the material with pronounced elasticity and time-dependent stress dissipation, enabling conformal adaptation to irregular wound contours and stable integration with bio-tissue interfaces [19]. As a result, the hydrogel is particularly suitable for wound management in high-load environments, such as diabetic ulcers, and is compatible with bioelectronic sensing systems.

3.3. *Bioelectronic sensing performance of GPGQ hydrogel*

Bioelectronic sensing performance is critical for detecting weak electromyography (EMG) signals elicited by muscle activity or electrical stimulation during wound healing [35]. Key requirements include a high signal-to-noise ratio, low impedance, stable adhesion, and conformal contact with irregular skin surfaces. Reliable performance under mechanical deformation, moisture, and movement is essential for accurate signal acquisition in dynamic wound environments. Electrochemical impedance spectroscopy (EIS) was used to characterize the electrical properties of GPGQ hydrogels in both native and dehydrated-rehydrated states. As shown in Figs. 3a–b and S5a, the native GPGQ hydrogel exhibited a small semicircular arc in the Nyquist plot and consistently low impedance ($< 10^3$ Ω) across the 1–100 Hz frequency range in the Bode plot, indicating low charge-transfer resistance and high ionic permeability. These advantageous characteristics arise from its interconnected, porous, and conductive network, as well as its hydrated ionic microenvironment, which collectively minimize signal transmission loss and enhance bioelectronic sensing sensitivity. Signal fidelity assessment (Figs. 3c–h and S5b–e) further demonstrated that GPGQ hydrogels faithfully transmit both square and sine waveforms across a broad frequency range (0.1 Hz to 100 kHz) with minimal distortion, highlighting their suitability for capturing a wide range of physiological electrical signals.

In multichannel EMG recordings (Figs. 3i and S5f), GPGQ hydrogel electrodes clearly captured periodic electrical pulses across five channels under varying grip forces (100 N, 200 N, and 350 N), as synchronized with a grip force sensor. The signal amplitude increased in a force-dependent manner, demonstrating high sensitivity and reliable fidelity in detecting bioelectrical activity. Time–frequency analysis of the CH3 channel (Fig. 3j) revealed periodic signal enhancements predominantly within the 0–300 Hz range, corresponding closely to the typical EMG frequency spectrum. The spectrogram displayed a distinct colour gradient, reflecting signal intensity, high temporal resolution, and the absence of artifacts or extraneous frequency components. These findings demonstrate that the GPGQ hydrogel offers excellent temporal resolution and spectral stability, enabling real-time monitoring of EMG frequency dynamics in the vicinity of wound regions. This capability is particularly advantageous for quantifying muscle activity levels and assessing rehabilitation progress [14]. The GPGQ hydrogel serves as a conformable, low-impedance bioelectronic interface that maintains high signal fidelity across a wide frequency range, even under mechanical deformation and in moist conditions. Its conductive, hydrated

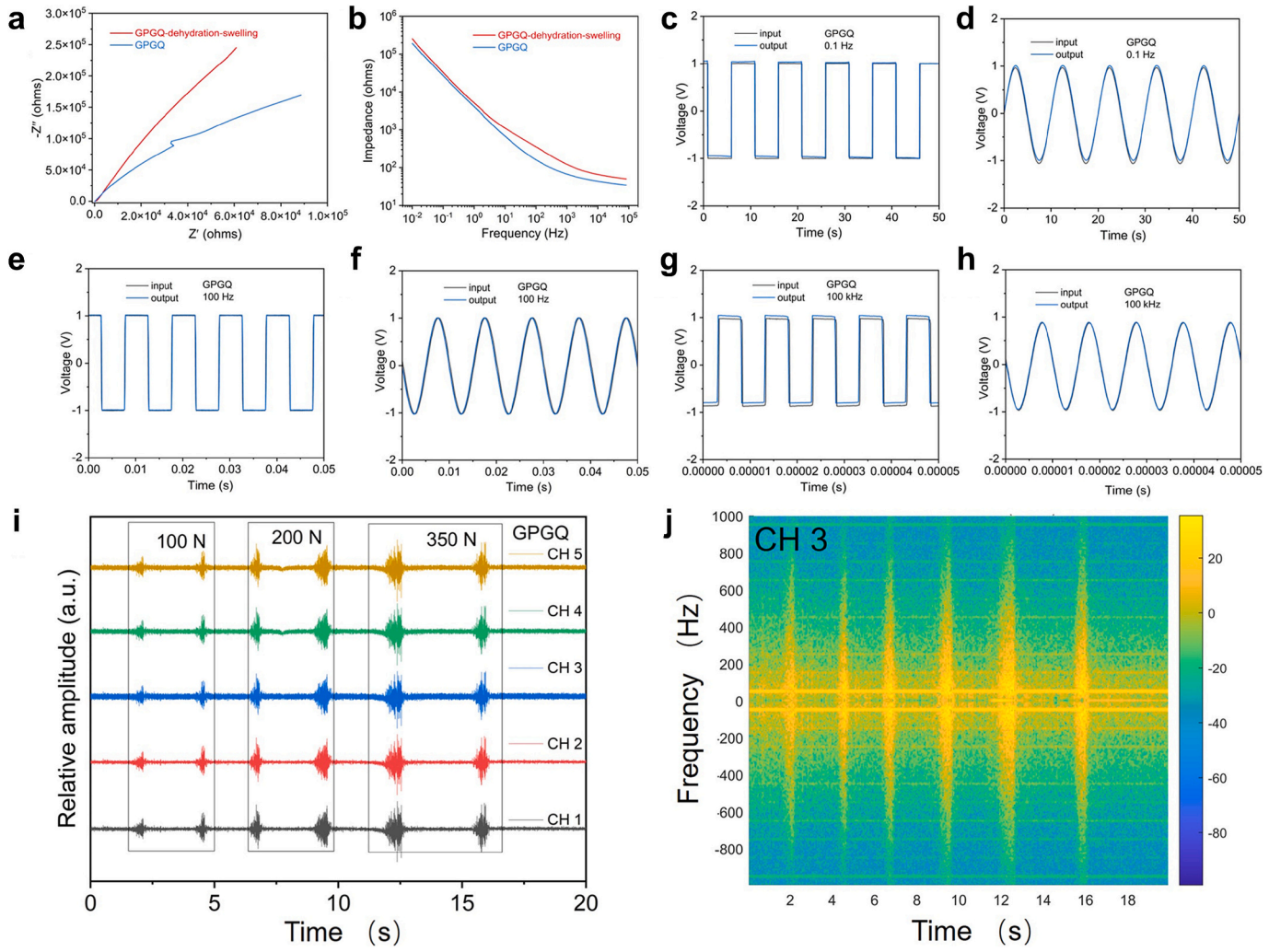

Fig. 3. Electrochemical and signal transmission properties of GPGQ hydrogel. a) Nyquist and b) Bode plots of GPGQ hydrogel from electrochemical impedance spectroscopy (EIS) measured in NaCl solution. c–h) Input and output voltage waveforms of GPGQ hydrogel at different frequencies. i) Continuous sEMG recording using GPGQ hydrogel under varying loading conditions (100 N, 200 N, 350 N) across multiple channels (CH 1–5). j) Time–frequency analysis of the GPGQ hydrogel signal from channel CH3.

microstructure ensures minimal signal distortion, enabling precise acquisition of physiologically relevant EMG signals. The material exhibits robust multichannel sensing capabilities with high temporal resolution, enabling real-time monitoring of muscle activity. These attributes make it a promising substitute for closed-loop wound monitoring and personalized rehabilitation applications.

3.4. In vitro biocompatibility, antioxidant, and antimicrobial activity of hydrogels

Biocompatibility is a fundamental requirement for wound dressings, reflecting their ability to function in contact with biological tissues without inducing adverse effects [36]. In this study, the cytocompatibility and hemocompatibility of GPGQ hydrogels were investigated to assess their potential for biomedical applications. As shown in Figs. 4a–b, human dermal fibroblasts cultured with GPGQ, PGQ, or PG hydrogels exhibited no significant cytotoxicity on day 1, with cell viability in all groups exceeding 90% and comparable to the control. By day 3, however, marked cell death was observed in the PG group, accompanied by a pronounced reduction in the proportion of viable cells, whereas cell viability in the GPGQ and PGQ groups remained above 90%. Quantitative analysis using the CCK-8 assay further confirmed that cell viability in the PG group was significantly lower than in the GPGQ and PGQ groups ($p < 0.01$), indicating inferior long-term cytocompatibility. The observed differential cytocompatibility can be attributed to the distinct compositions of the hydrogels. The superior performance of PGQ relative to PG is likely due to the incorporation of QAC. The cationic nature of QAC's quaternary ammonium groups is known to promote initial cell attachment and membrane stability through electrostatic interactions, which could explain the enhanced cell survival. Furthermore, as demonstrated in the mechanical characterization (Fig. 2, S4), the incorporation of QAC strengthens the hydrogel network through enhanced cross-linking. A more stable network is less prone to disintegration during culture, thereby reducing the potential release of degradation products that could exert mild cytotoxicity over time, as may occur in the less stable PG hydrogel. The GPGQ hydrogel, which incorporates GSE in addition to QAC, demonstrated the highest cytocompatibility, suggesting a potential additional benefit from GSE. Thus, the gradation in cytocompatibility (GPGQ > PGQ > PG) reflects the cumulative advantages of the compositional modifications to the base PVA-gelatin matrix.

Furthermore, all hydrogels exhibited good hemocompatibility. Hemolysis assays showed no significant hemolysis when red blood cells contacted PG, PGQ, or GPGQ hydrogels. Notably, all hydrogel groups exhibited hemolysis ratios below 5%, which meets the international standard for blood-contacting biomaterials. Both qualitative

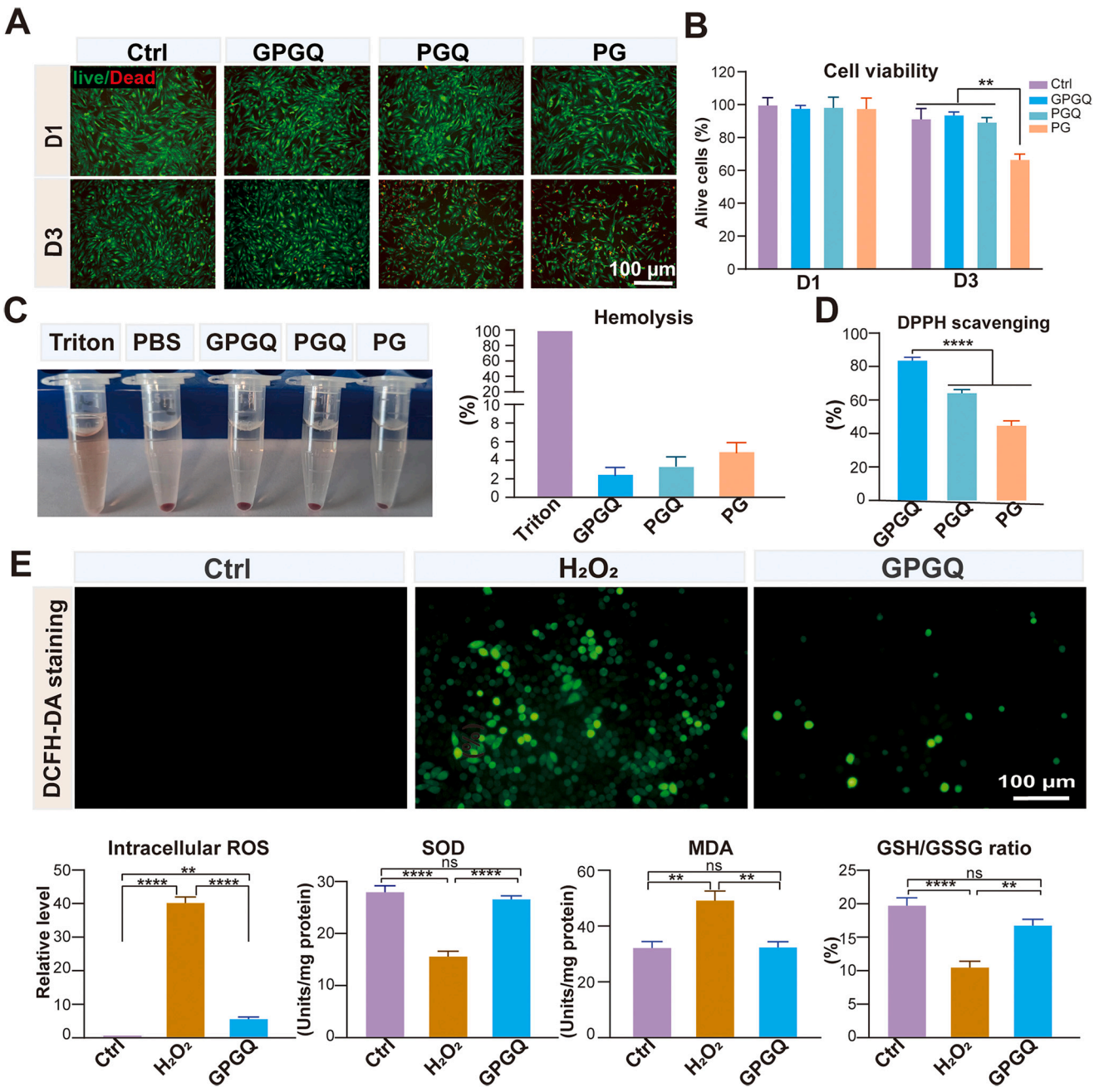

Fig. 4. In vitro biocompatibility and antioxidant activity of the hydrogels. a) Live/Dead staining of human dermal fibroblasts after 1 and 3 days of culture with PG, PGQ, and GPGQ hydrogels. b) Viability of L929 cells treated with PG, PGQ, and GPGQ hydrogels for 1 and 3 days. c) Hemolytic evaluation of PG, PGQ, and GPGQ hydrogels, showing both photographic documentation and quantitative hemolysis ratio (%). d) DPPH radical scavenging activity of PG, PGQ, and GPGQ hydrogels. e) Assessment of antioxidative effects of GPGQ hydrogel on H_2O_2-stimulated cells, including representative fluorescence images of intracellular ROS (DCFH-DA), f) quantitative fold-change in ROS level, and concentrations of SOD, MDA, and GSH/GSSG ratio. All data are presented as mean ± 95% CI ($n = 6$).

observations and quantitative hemolysis rate measurements consistently supported this conclusion (Fig. 4c), indicating that these materials possess a good safety profile for blood-contact applications.

Excessive ROS impede wound healing by causing oxidative stress and chronic inflammation. Antioxidant hydrogels can scavenge ROS, reducing damage and promoting tissue regeneration, which is crucial in chronic wounds like diabetic ulcers [37]. Assessing antioxidant capacity is therefore vital for the development of advanced hydrogel-based therapies that create a pro-regenerative microenvironment. Antioxidant efficiency, crucial for scavenging ROS and protecting cells, was most pronounced in the GPGQ group, which demonstrated the highest DPPH radical scavenging rate ($p < 0.0001$) (Fig. 4d). Upon H_2O_2 stimulation, L929 cells showed a substantial rise in intracellular ROS; however, treatment with GPGQ hydrogel significantly attenuated ROS levels, indicating effective protection against oxidative damage (Fig. 4e). Mechanistically, GPGQ hydrogel helped restore redox homeostasis by upregulating superoxide dismutase (SOD) activity, reducing malondialdehyde (MDA) content, and maintaining a higher GSH/GSSG ratio, thereby counteracting H_2O_2-induced oxidative stress (Fig. 4f).

In terms of antimicrobial performance, as shown in Fig. S6, GPGQ hydrogels exhibited the most potent inhibitory effects against both *E. coli* and *S. aureus*, as evidenced by significantly larger inhibition zone diameters compared to those of the PGQ and PG groups. The PGQ

hydrogel also showed greater antibacterial activity than the PG group, which can be attributed to the incorporation of QAC. QAC exerts its bactericidal effect through electrostatic interactions between its positively charged ammonium groups and the negatively charged bacterial cell membranes, leading to membrane disruption and leakage of cell contents [38]. The further enhanced antibacterial efficacy of the GPGQ hydrogel is attributed to the co-presence of GSE. GSE is rich in polyphenols, notably proanthocyanidins, which are known to damage bacterial membranes and inhibit biofilm formation [39]. The combination of QAC and GSE in the GPGQ hydrogel thus creates a synergistic antibacterial effect, resulting in superior performance. In addition, MIC values determined from hydrogel extracts further confirmed these findings (Supplementary Table S1). GPGQ extracts showed MICs of approximately 1.0–2.5 mg/mL for *S. aureus* and 2.5–5.0 mg/mL for *E. coli*, indicating effective inhibition of bacterial growth. PGQ extracts exhibited moderate antibacterial activity, with higher MIC values, whereas PG extracts showed minimal inhibition at the tested concentrations. These data quantitatively support the broad-spectrum antibacterial efficacy of the GPGQ hydrogel and reinforce its potential application in diabetic wound management.

These results demonstrate that the GPGQ hydrogel possesses not only excellent biocompatibility and antioxidant functionality but also enhanced and broad-spectrum antimicrobial efficacy, highlighting its significant potential for promoting healing in diabetic wounds by mitigating infection and oxidative damage, key barriers to recovery in hyperglycemic environments.

3.5. *In vitro enhancement of migration and angiogenesis by hydrogels*

Wound healing is a complex physiological process involving multiple cellular events, with cell migration and angiogenesis being crucial for re-epithelialization and tissue regeneration [40]. As a class of biomaterials, hydrogels can exert paracrine effects via their extracts to impact the behavior of cells participating in wound healing [41], so we examined how extracts from different hydrogels (GPGQ, PGQ, and PG) affect the migration of human dermal fibroblasts and the angiogenic potential of

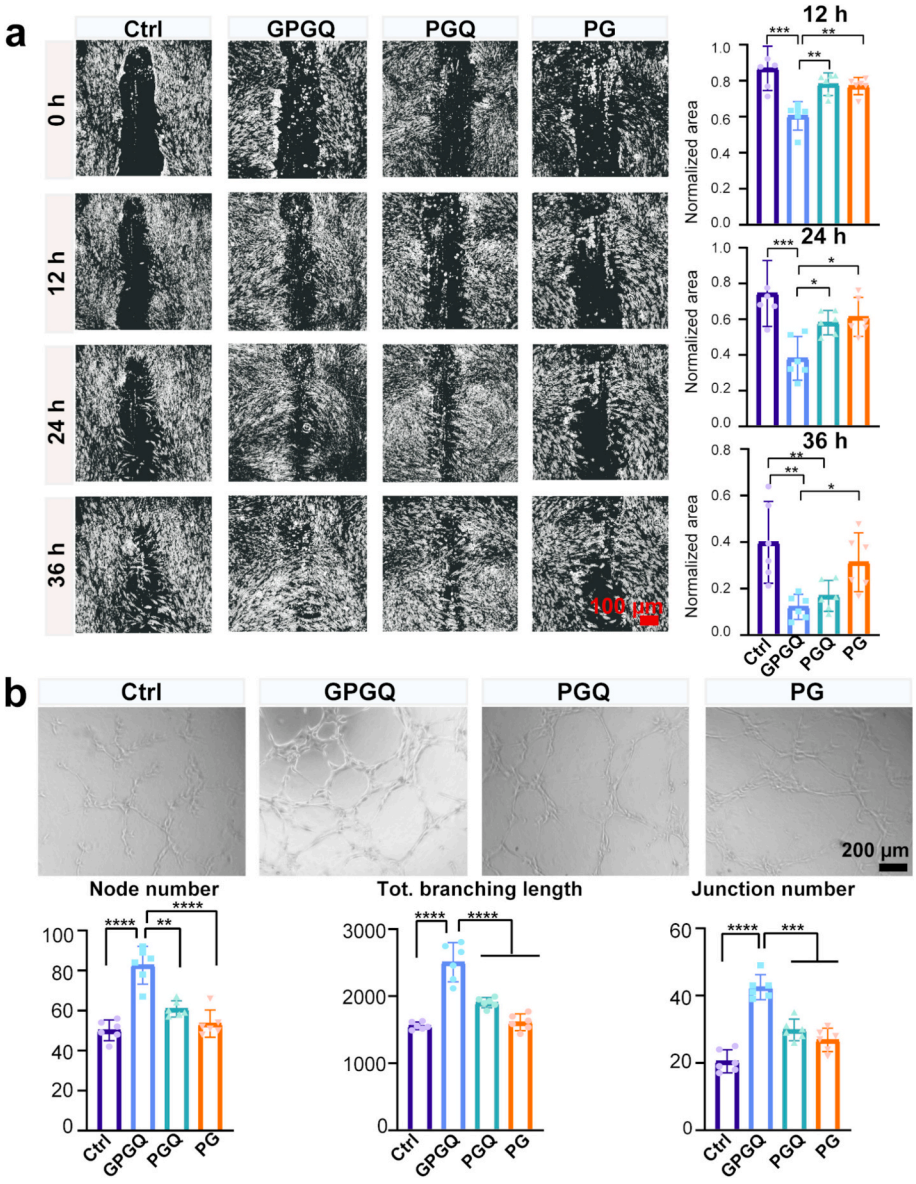

Fig. 5. GPGQ hydrogel promoted cell migration and angiogenesis in vitro. a) Scratch assay showing the migration of fibroblasts treated with extracts from GPGQ, PGQ, and PG hydrogels at 0, 12, 24, and 36 h (representative images shown). b) The normalized wound area (relative to the initial wound area at 0 h) was quantified and compared among groups at 12, 48, and 72 h. c) Tube formation assay of HUVECs after treatment with different hydrogels. d) The number of nodes, total branching length, and junctions were quantified in each group. Data are presented as mean ± 95% CI ($n = 6$).

human umbilical vein endothelial cells (HUVECs). For evaluating cell migration, a scratch assay was performed on human dermal fibroblasts treated with extracts from these hydrogels, and representative images at 0, 12, 24, and 36 h (Fig. 5a) depicted the dynamic wound closure process; quantification of the normalized wound area (relative to the initial wound area at 0 h) at 12, 48, and 72 h showed that the GPGQ hydrogel extract group had significantly faster wound closure, with the normalized wound area in the GPGQ group being notably smaller than that in the PGQ and PG groups at 12 h, a pattern that continued at 48 h and became more pronounced at 72 h (Fig. 5b), indicating GPGQ hydrogel

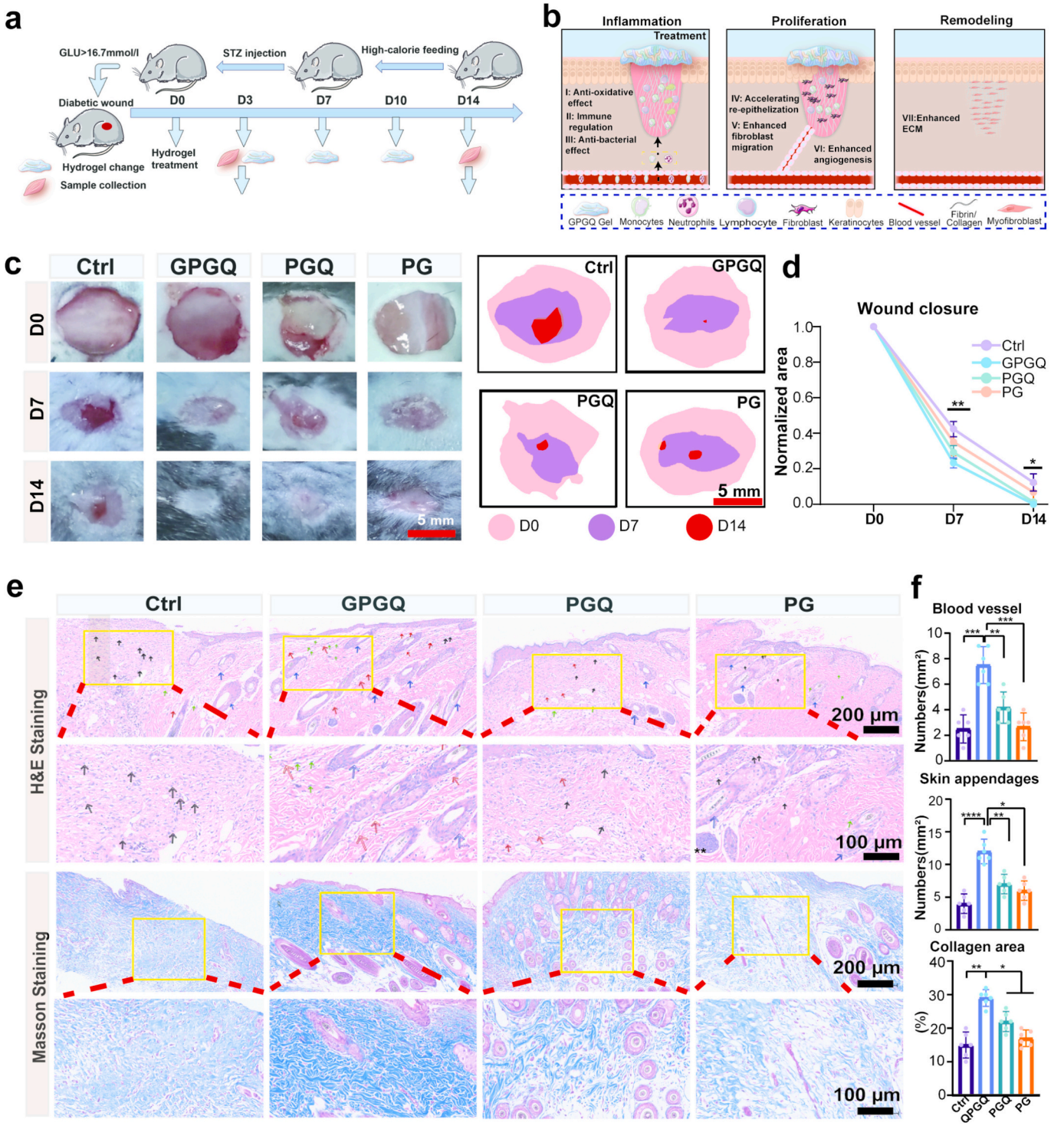

Fig. 6. Therapeutic efficacy of GPGQ hydrogel in a diabetic mouse wound model. a) Schematic timeline of the animal experiment evaluating the therapeutic effect of hydrogels; STZ: Streptozocin; GLU: Glucose. b) Proposed mechanisms of GPGQ hydrogel in promoting diabetic wound healing through multiple stages: inflammation, proliferation, and remodeling. c) Representative wound photographs on days 0, 7, and 14, and quantitative analysis of wound closure from different treatment groups. d) Normalized wound area was calculated relative to day 0. e) Histological analysis of wound tissues on day 14 using H&E and Masson's trichrome staining. Black arrow, inflammatory cell; green arrow, fibroblast; blue arrow, hair follicle or sebaceous gland; red arrow, blood vessel. f) Histological analysis of neovascular density, numbers of de novo skin appendages, and relative collagen content, based on H&E and Masson staining. Data are mean ± 95% CI ($n = 6$). (For interpretation of the references to colour in this figure legend, the reader is referred to the web version of this article.)

extract promoted fibroblast migration in both early and late stages of simulated wound healing. In the tube formation assay using hUVECs (Fig. 5c), treatment with GPGQ hydrogel extract brought about remarkable improvements in angiogenic parameters: the number of nodes (representing points where tubes intersect or branch), total branching length (a measure of tube network formation extent), and number of junctions (critical for forming a functional vascular network) were all significantly higher in the GPGQ group compared to the PGQ and PG groups (Fig. 5d). Enhanced fibroblast migration induced by GPGQ hydrogel extract is highly significant for wound healing, as faster fibroblast migration to the wound site can accelerate extracellular matrix deposition and granulation tissue formation essential for wound closure [42], while the pro-angiogenic effects observed in HUVECs treated with GPGQ hydrogel extract are also vital since angiogenesis supplies oxygen and nutrients to healing tissue, removes waste products, and facilitates the infiltration of various repair-related cells [43]. Compared with PGQ and PG hydrogel extracts, GPGQ hydrogel extract showed superior ability in promoting both cell migration and angiogenesis—suggesting its chemical composition or physical properties may enable secretion of more effective stimulatory factors (e.g., growth factors, cytokines, other bioactive molecules) for these cellular processes—and significantly enhances human dermal fibroblast migration and HUVECs angiogenesis in vitro; these paracrine effects critically regulate wound healing, supporting GPGQ hydrogel's potential as a wound-healing biomaterial via modulating migration- and angiogenesis-related cellular activities.

3.6. *In vivo promotion of diabetic wound healing by hydrogels*

Following promising in vitro results, the efficacy of the hydrogels was further evaluated in a full-thickness diabetic wound-healing model (Figs. 6a,b). Diabetes was induced in mice using a combination of a high-fat diet and streptozotocin (STZ) injections, with hyperglycemia confirmed by sustained blood glucose levels above 16.7 mmol/L for four weeks prior to wounding. Full-thickness skin defects were created on the dorsal skin and treated with GPGQ, PGQ, or PG hydrogels, which were refreshed every three days to maintain bioactivity; the control group received 3 M Tegaderm film as a standard wound dressing. The wound closure process was monitored over 14 days using macroscopic imaging and planimetric analysis. Photographic and quantitative analyses revealed that all hydrogel-treated groups exhibited enhanced wound healing compared to the control. Notably, the GPGQ group showed the most substantial improvement, with significantly reduced wound areas observable as early as day 7 (approximately 78% closure vs. 58% in control) and nearly complete closure (over 95%) by day 14 (Figs. 6c,d). In contrast, approximately 20% of the wound area remained unhealed in the control group at the endpoint. These in vivo findings align well with the in vitro scratch assay, confirming the strong pro-migratory effect of GPGQ hydrogel.

Histological assessment with H&E and Masson's trichrome staining on day 14 provided further insight into the quality of healing and tissue architecture. All hydrogel groups showed reduced inflammatory cell infiltration, with the GPGQ group exhibiting the most pronounced decrease (black arrows, Fig. 6e), suggesting effective immunomodulation. Furthermore, the GPGQ-treated wounds displayed markedly enhanced tissue regeneration, including the reappearance of skin appendages such as hair follicles and sebaceous glands (blue arrows), increased blood vessel density (red arrows), and a higher abundance of fibroblasts (green arrows), indicating robust granulation tissue formation and re-epithelialization. Masson's trichrome staining revealed better-organized, denser collagen deposition and increased alignment in the GPGQ group, suggesting improved extracellular matrix remodeling and maturation, which are crucial for restoring skin integrity and mechanical strength. To quantitatively assess these observations, histological analyses were conducted. Neovascular density, quantified by counting blood vessels per unit area, was markedly elevated in wounds treated with GPGQ ($p < 0.01$, Fig. 6f). Additionally, the number of newly formed skin appendages, including hair follicles and sebaceous glands, was significantly higher in the GPGQ group ($p < 0.05$). Relative collagen content was measured by image analysis of Masson's trichrome-stained sections, revealing a significant increase in the GPGQ group compared to PGQ, PG, and control groups ($p < 0.01$). These quantitative results corroborate the qualitative histological findings and demonstrate that GPGQ hydrogel treatment substantially enhances extracellular matrix remodeling, angiogenesis, and skin appendage regeneration, thereby indicating improved wound-healing quality. Importantly, no signs of systemic toxicity were observed in any hydrogel group, as histological examination of major organs (heart, liver, spleen, lung, and kidney) at day 40 revealed no apparent histological abnormalities or pathological changes, such as necrosis, fibrosis, or abnormal inflammatory infiltration (Fig. S7), indicating good biosafety and biocompatibility of the hydrogels. The GPGQ hydrogel conforms effectively to wounds with diverse geometries and surface contours, as illustrated in Fig. S8. This adaptive behavior facilitates uniform coverage and maintains stable contact with the wound bed under movement, ensuring consistent delivery of bioactive components and physical support throughout the healing process.

The accelerated and improved healing conferred by GPGQ hydrogel, as summarized in the proposed mechanism (Fig. 6b), can be attributed to its multi-stage regulatory functions, which modulate inflammation, promote angiogenesis and fibroblast activation, and facilitate collagen maturation. Future research should focus on elucidating the molecular signaling pathways underlying the multidimensional regenerative effects of GPGQ hydrogels.

3.7. *Immunomodulatory and angiogenic properties of hydrogels*

Regulating the inflammatory response is essential for effective wound healing, particularly in diabetic wounds where prolonged inflammation often impedes recovery [44]. Pro-inflammatory cytokines such as IL-1β, IL-6, and TNF-α initiate immune cell recruitment and debris clearance in the early phase, while anti-inflammatory mediators, including IL-10 and TGF-β, facilitate angiogenesis and tissue remodeling in later stages. Achieving a balanced immune response is critical to prevent excessive inflammation and support structured tissue repair [45]. Immunofluorescence staining and ELISA results indicated that on day 3, GPGQ hydrogel treatment significantly reduced the levels of pro-inflammatory cytokines (IL-1β, IL-6, TNF-α) and elevated the levels of anti-inflammatory cytokines (IL-10, TGF-β) compared to the PGQ, PG, and control groups (Fig. 7). This modulation of the immune microenvironment was sustained through day 14 (Fig. S9), demonstrating GPGQ's capacity to promote a transition from pro-inflammatory to pro-regenerative states.

Angiogenesis is a critical process in wound healing, ensuring the delivery of oxygen and essential nutrients to the wound bed and thereby facilitating tissue regeneration [43]. To evaluate angiogenic activity, we examined the expression of two well-established markers: CD31, which is specifically expressed on endothelial cells and serves as a reliable indicator of microvessel density and nascent vascular structures, and VEGF, a key growth factor that regulates endothelial cell proliferation, migration, and the formation of new blood vessels. Immunofluorescence staining revealed that both CD31 and VEGF levels were significantly elevated in the GPGQ group compared to the PGQ and PG groups, all of which exceeded the levels observed in the control group (Fig. 7a). The GPGQ-treated wounds exhibited obvious and continuous $CD31^+$ vascular structures, as well as pronounced VEGF expression in the perivascular and granulation tissue areas. Quantitative analysis further demonstrated that the expression levels of CD31 and VEGF in the GPGQ group were approximately 4-fold and 3-fold higher, respectively, than those in the control group (Fig. 7b). Additionally, ELISA results indicated that VEGF secretion in the GPGQ group was nearly double that of the control group and significantly higher than in the other hydrogel

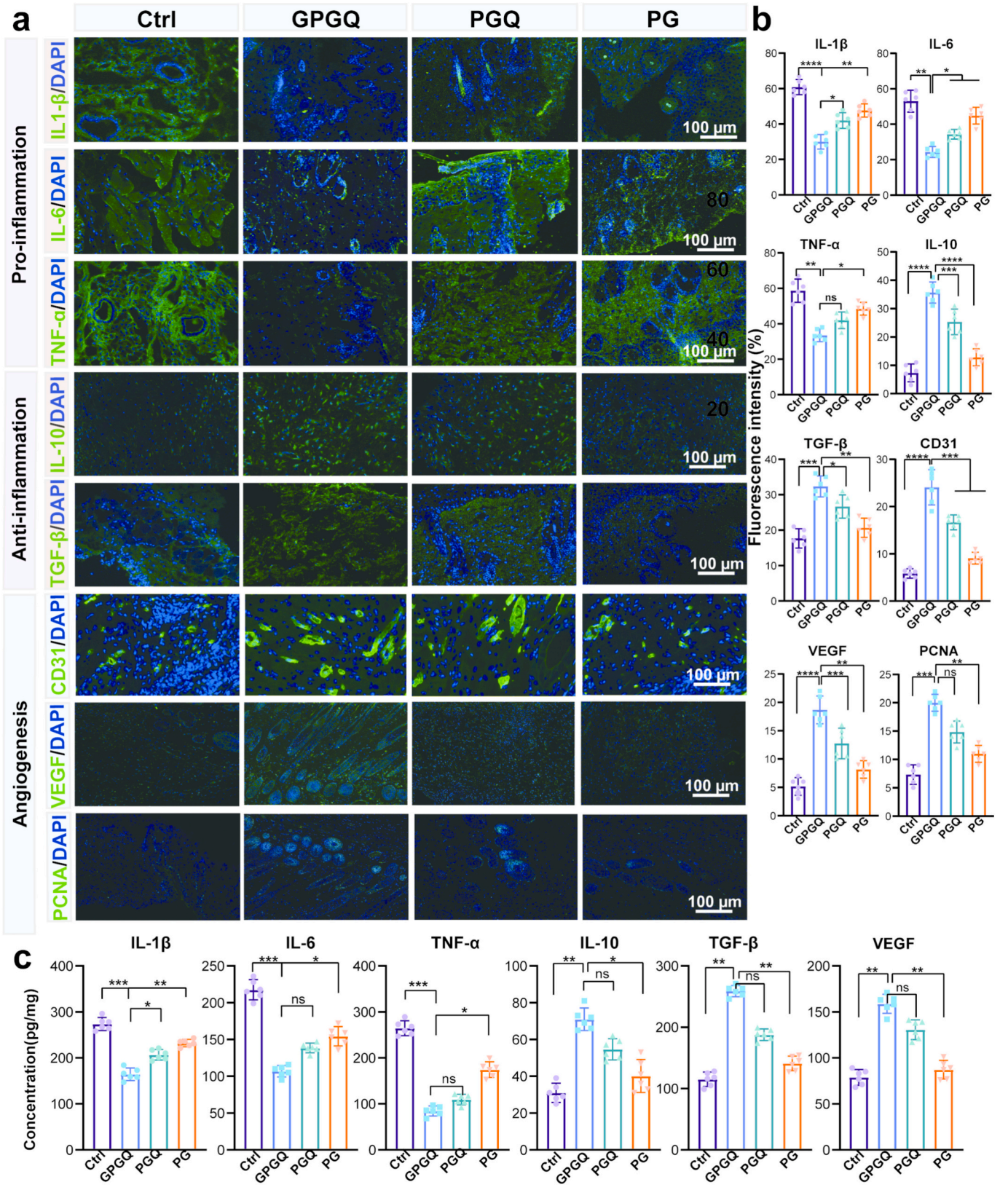

Fig. 7. Immunomodulatory and angiogenic properties of hydrogels in diabetic wounds. a) Immunofluorescence staining of pro-inflammatory cytokines (IL-1β, IL-6, TNF-α) and anti-inflammatory cytokines (IL-10, TGF-β) in wound tissues on day 3, and angiogenesis markers (CD31, VEGF) along with the proliferation marker PCNA on day 14. Nuclei were counterstained with DAPI (blue). b) Quantitative analysis of fluorescence intensity for the markers shown in (a). c) Concentrations of inflammation- and angiogenesis-related chemokines/cytokines in wound tissues as determined by ELISA. Data are presented as mean ± 95% CI ($n = 6$). (For interpretation of the references to colour in this figure legend, the reader is referred to the web version of this article.)

groups (Fig. 7c), reinforcing the protein-level validation of the enhanced angiogenic response. Cell proliferation, another vital component of wound repair, was assessed by measuring PCNA (Proliferating Cell Nuclear Antigen) expression, a marker closely associated with active cell division. All hydrogel treatments enhanced PCNA expression compared to the control group (Fig. 7a). Notably, the GPGQ group demonstrated the most significant pro-proliferative effect, exhibiting a nearly 4-fold increase in PCNA signal, suggesting markedly accelerated cellular replication during tissue regeneration (Fig. 7b). Thus, while all hydrogels promoted angiogenesis and cell proliferation, the GPGQ hydrogel exerted the most significant impact, effectively enhancing vascularization and cellular turnover—key processes for successful wound healing.

4. Conclusion

Herein, we report a GPGQ mechanoadaptive conductive hydrogel ~~(GPGQ)~~ designed for the management of diabetic chronic wounds, integrating tunable mechanical properties, conductivity, and bioactive functions. The hydrogel exhibits rehydratable mechanical behavior, transitioning from softness in the hydrated state (0.10 MPa tensile strength, 0.20 MPa compressive strength) to greater strength upon dehydration (0.25 MPa tensile strength, 2.3 MPa compressive strength), with flexibility recovery exceeding 90% after rehydration. Tissue adhesion reached 60 kPa to porcine skin, and the material's porous network (20–80 μm) supported cell integration and ion transport. With an electrochemical impedance below 10^3 Ω, the hydrogel permitted stable sEMG recording across a 0.1 Hz–100 kHz bandwidth, enabling the monitoring of muscle activity signals under varying pressure conditions. Bioactive components derived from GSE reduced ROS, modulated cytokine levels (lowering IL-1β, IL-6, and TNF-α; raising IL-10 and TGF-β), and supported redox homeostasis. Collectively, the in vitro and in vivo tests confirmed that GPGQ promotes wound healing by enhancing fibroblast migration, angiogenesis, and collagen deposition, thereby accelerating wound closure. These results demonstrate that GPGQ contributes to diabetic wound healing through a synergistic combination of mechanical, electrical, and biochemical modes of action.

It is worth noting that the current findings are based on a rodent model, and the long-term performance of GPGQ warrants further evaluation. Future investigations will therefore focus on validation in larger animal models and the exploration of extended monitoring capabilities.

In summary, this study establishes GPGQ as a multifunctional theranostic dressing for diabetic wound care, supporting healing processes and enabling electrophysiological monitoring.

CRediT authorship contribution statement

Guoqiang Ren: Writing – original draft, Formal analysis, Data curation. **Jingyun Ma:** Writing – original draft, Formal analysis, Data curation. **Qiuyue Peng:** Writing – original draft, Formal analysis, Data curation. **Pengfei Liu:** Writing – original draft, Formal analysis, Data curation. **Xiaobo Wang:** Formal analysis, Data curation. **Da Li:** Formal analysis, Data curation. **Yuesheng Zhang:** Formal analysis, Data curation. **Chaonan He:** Formal analysis, Data curation. **Chen Huang:** Data curation. **Honghua Ye:** Data curation. **Yavuz Nuri Ertas:** Writing – review & editing, Visualization, Supervision. **Qingbo Xu:** Writing – review & editing, Supervision. **Jiangfang Lian:** Writing – review & editing, Supervision. **Mingming Hao:** Writing – review & editing, Supervision, Funding acquisition.

Funding

This work was support by the China Postdoctoral Science Foundation (2024M762614, 2025M772891), the Postdoctoral Fellowship Program (Grad C) of China Postdoctoral Science Foundation (GZC20250355), the 2023-SZZ Key Specialized Construction Project in Cardiology Department of Zhejiang Province (2023-SZZ), the Natural Science Foundation of Zhejiang Province (LQN26H150010), Ningbo Key Research and Development Program (2024Z232), and Ningbo Key Research and Development Program (2024Z210), Jiangsu Province's Outstanding Postdoctoral Program Funding (2025ZB406), the National Natural Science Foundation of China (62501591). Y.N.E. acknowledges support from the Turkish Academy of Sciences Distinguished Young Scientist Award (TÜBA-GEBİP) and Scientific and Technological Research Council of Türkiye (TÜBİTAK) Incentive Award.

Declaration of competing interest

The authors declare that they have no known competing financial interests or personal relationships that could have influenced the work reported in this paper.

Appendix A. Supplementary data

Supplementary data to this article can be found online at https://doi.org/10.1016/j.cej.2026.174639.

Data availability

Data will be made available on request.

References

[1] S. Schreml, M. Berneburg, The global burden of diabetic wounds, Br. J. Dermatol. 176 (4) (2017) 845–846, https://doi.org/10.1111/bjd.15254.
[2] F. Huang, X. Lu, Y. Yang, Y. Yang, Y. Li, L. Kuai, B. Li, H. Dong, J. Shi, Microenvironment-based diabetic foot ulcer nanomedicine, Adv Sci (Weinh) 10 (2) (2023) e2203308, https://doi.org/10.1002/advs.202203308.
[3] A. Wahlsten, A. Stracuzzi, I. Luchtefeld, G. Restivo, N. Lindenblatt, C. Giampietro, A.E. Ehret, E. Mazza, Multiscale mechanical analysis of the elastic modulus of skin, Acta Biomater. 170 (2023) 155–168, https://doi.org/10.1016/j.actbio.2023.08.030.
[4] C.M.O. Volpe, P.H. Villar-Delfino, P.M.F. Dos Anjos, J.A. Nogueira-Machado, Cellular death, reactive oxygen species (ROS) and diabetic complications, Cell Death Dis. 9 (2) (2018) 119, https://doi.org/10.1038/s41419-017-0135-z.
[5] N.N. Mahmoud, S. Hamad, S. Shraim, Inflammation-modulating biomedical interventions for diabetic wound healing: an overview of preclinical and clinical studies, ACS Omega 9 (45) (2024) 44860–44875, https://doi.org/10.1021/acsomega.4c02251.
[6] G. Wang, Z. Lin, Y. Li, L. Chen, S.K. Reddy, Z. Hu, L.A. Garza, Colonizing microbiota is associated with clinical outcomes in diabetic wound healing, Adv. Drug Deliv. Rev. 194 (2023) 114727, https://doi.org/10.1016/j.addr.2023.114727.
[7] N. Yadu, M. Singh, D. Singh, S. Keshavkant, Mechanistic insights of diabetic wound: healing process, associated pathways and microRNA-based delivery systems, Int. J. Pharm. 670 (2025) 125117, https://doi.org/10.1016/j.ijpharm.2024.125117.
[8] Z. Zheng, J. Yang, W. Zheng, Z. Chu, W. Wang, H. Qian, L. Xu, Comprehensive management of diabetic ulceration: strategies and perspectives, J. Control. Release 385 (2025) 114058, https://doi.org/10.1016/j.jconrel.2025.114058.
[9] J.A. Mullin, E. Rahmani, K.L. Kiick, M.O. Sullivan, Growth factors and growth factor gene therapies for treating chronic wounds, Bioeng. Transl. Med. 9 (3) (2024) e10642, https://doi.org/10.1002/btm2.10642.
[10] S. Ji, X. Liu, J. Huang, J. Bao, Z. Chen, C. Han, D. Hao, J. Hong, D. Hu, Y. Jiang, S. Ju, H. Li, Z. Li, G. Liang, Y. Liu, G. Luo, G. Lv, X. Ran, Z. Shi, J. Tang, A. Wang, G. Wang, J. Wang, X. Wang, B. Wen, J. Wu, H. Xu, M. Xu, X. Ye, L. Yuan, Y. Zhang, S. Xiao, Z. Xia, Consensus on the application of negative pressure wound therapy of diabetic foot wounds, Burns Trauma 9 (2021) tkab018, https://doi.org/10.1093/burnst/tkab018.
[11] Z. Xu, S. Han, Z. Gu, J. Wu, Advances and impact of antioxidant hydrogel in chronic wound healing, Adv. Healthc. Mater. 9 (5) (2020) e1901502, https://doi.org/10.1002/adhm.201901502.
[12] S. Khattak, I. Ullah, M.T. Yousaf, S. Ullah, H. Yousaf, Y. Li, H. Jin, J. Shen, H.T. Xu, Advancements in hydrogels: a comprehensive review of natural, synthetic, and hybrid innovations for wound healing, Int. J. Biol. Macromol. 327 (Pt 1) (2025) 147270, https://doi.org/10.1016/j.ijbiomac.2025.147270.
[13] C.M. Lai, W.J. Chen, Y. Qin, D. Xu, Y.K. Lai, S.H. He, Innovative hydrogel design: tailoring immunomodulation for optimal chronic wound recovery, Adv Sci (Weinh) 12 (2) (2025) e2412360, https://doi.org/10.1002/advs.202412360.
[14] H. Cao, L. Duan, Y. Zhang, J. Cao, K. Zhang, Current hydrogel advances in physicochemical and biological response-driven biomedical application diversity, Signal Transduct. Target. Ther. 6 (1) (2021) 426, https://doi.org/10.1038/s41392-021-00830-x.
[15] M.H. Norahan, S.C. Pedroza-Gonzalez, M.G. Sanchez-Salazar, M.M. Alvarez, G. Trujillo de Santiago, Structural and biological engineering of 3D hydrogels for

wound healing, Bioact. Mater. 24 (2023) 197–235, https://doi.org/10.1016/j.bioactmat.2022.11.019.
[16] J. Ma, J. Zhong, F. Sun, B. Liu, Z. Peng, J. Lian, X. Wu, L. Li, M. Hao, T. Zhang, Hydrogel sensors for biomedical electronics, Chem. Eng. J. 481 (2024), https://doi.org/10.1016/j.cej.2023.148317.
[17] S.Y. Chen, T. Feng, Z.Q. Wu, N. Bao, Recent applications and advancement of conductive hydrogels in biosensing, bioelectronics and bioengineering, Mikrochim. Acta 192 (4) (2025) 263, https://doi.org/10.1007/s00604-025-07123-y.
[18] Y. Fang, Y. Han, L. Yang, R.K. Kankala, S. Wang, A. Chen, C. Fu, Conductive hydrogels: intelligent dressings for monitoring and healing chronic wounds, Regener. Biomater. 12 (2025) rbae127, https://doi.org/10.1093/rb/rbae127.
[19] T.K.N. Duong, T.T. Truong, T.N.L. Phan, T.X. Nguyen, V.H.M. Doan, T.T. Vo, J. Choi, U. Pal, P. Dhar, B. Lee, J. Oh, S. Mondal, Hydrogel-based smart materials for wound healing and sensing, Aggregate 6 (6) (2025), https://doi.org/10.1002/agt2.70047.
[20] M. Kumar, P. Sethi, J. Shiekmydeen, S. Rastogi, S. Mahmood, S. Chopra, S. Thomas, D. Kumar, A. Bhatia, A recent review on smart sensor-integrated wound dressings: real-time monitoring and on-demand therapeutic delivery, Int. J. Biol. Macromol. 313 (2025) 144251, https://doi.org/10.1016/j.ijbiomac.2025.144251.
[21] Y. Zhong, F. Seidi, C. Li, Z. Wan, Y. Jin, J. Song, H. Xiao, Antimicrobial/biocompatible hydrogels dual-reinforced by cellulose as Ultrastretchable and rapid self-healing wound dressing, Biomacromolecules 22 (4) (2021) 1654–1663, https://doi.org/10.1021/acs.biomac.1c00086.
[22] X. Han, C. Saengow, L. Ju, W. Ren, R.H. Ewoldt, J. Irudayaraj, Exosome-coated oxygen nanobubble-laden hydrogel augments intracellular delivery of exosomes for enhanced wound healing, Nat. Commun. 15 (1) (2024) 3435, https://doi.org/10.1038/s41467-024-47696-5.
[23] Z. Sun, Q. Ou, C. Dong, J. Zhou, H. Hu, C. Li, Z. Huang, Conducting polymer hydrogels based on supramolecular strategies for wearable sensors, Exploration (Beijing) 4 (5) (2024) 20220167, https://doi.org/10.1002/EXP.20220167.
[24] S. Zhang, T. Jiang, M. Li, H. Sun, H. Wu, W. Wu, Y. Li, H. Jiang, Graphene-based wound dressings for wound healing: mechanism, technical analysis, and application status, ACS Biomater. Sci. Eng. 10 (11) (2024) 6790–6813, https://doi.org/10.1021/acsbiomaterials.4c01142.
[25] Y. Nie, C. Hu, X. Huang, H. Zeng, Z. Wang, J. Liang, J. Wang, Accelerating wound healing through a Mechano-electric synergistic conductive hydrogel, ACS Appl. Bio Mater. 8 (6) (2025) 5183–5193, https://doi.org/10.1021/acsabm.5c00523.
[26] F. Zhang, H. Zhang, S. Wang, M. Gao, K. Du, X. Chen, Y. Lu, Q. Hu, A. Du, S. Du, J. Wang, K. Shi, Z. Chen, Z. Li, Z. Li, J. Xiao, A dynamically phase-adaptive regulating hydrogel promotes ultrafast anti-fibrotic wound healing, Nat. Commun. 16 (1) (2025) 3738, https://doi.org/10.1038/s41467-025-58987-w.
[27] Y. Shin, H.S. Lee, Y.J. Hong, S.H. Sunwoo, O.K. Park, S.H. Choi, D.H. Kim, S. Lee, Low-impedance tissue-device interface using homogeneously conductive hydrogels chemically bonded to stretchable bioelectronics, Sci. Adv. 10 (12) (2024) eadi7724, https://doi.org/10.1126/sciadv.adi7724.
[28] E.C. Lloyd, S. Dhakal, S. Amini, R. Alhasan, P. Fratzl, D.R. Tree, S. Morozova, R. J. Hickey, Porous hierarchically ordered hydrogels demonstrating structurally dependent mechanical properties, Nat. Commun. 16 (1) (2025) 3792, https://doi.org/10.1038/s41467-025-59171-w.
[29] T. Maeda, S. Tajima, M. Suto, K. Murai, Analysis of permeation and release behavior based on structural differences in the gelatin network within hydrogels, Macromol. Biosci. (2025) e00628, https://doi.org/10.1002/mabi.202400628.
[30] B. Yin, M. Gosecka, M. Bodaghi, D. Crespy, G. Youssef, J.M. Dodda, S.H.D. Wong, A.B. Imran, M. Gosecki, A. Jobdeedamrong, M. Afzali Naniz, A. Zolfagharian, Engineering multifunctional dynamic hydrogel for biomedical and tissue regenerative applications, Chem. Eng. J. 487 (2024), https://doi.org/10.1016/j.cej.2024.150403.
[31] X. Lin, X. Zhao, C. Xu, L. Wang, Y. Xia, Progress in the mechanical enhancement of hydrogels: fabrication strategies and underlying mechanisms, J. Polym. Sci. 60 (17) (2022) 2525–2542, https://doi.org/10.1002/pol.20220154.
[32] C. Wang, E. Shirzaei Sani, C.D. Shih, C.T. Lim, J. Wang, D.G. Armstrong, W. Gao, Wound management materials and technologies from bench to bedside and beyond, Nat. Rev. Mater. 9 (8) (2024) 550–566, https://doi.org/10.1038/s41578-024-00693-y.
[33] B. Liu, H. Li, F. Meng, Z. Xu, L. Hao, Y. Yao, H. Zhu, C. Wang, J. Wu, S. Bian, W. W. Lu, W. Liu, H. Pan, X. Zhao, 4D printed hydrogel scaffold with swelling-stiffening properties and programmable deformation for minimally invasive implantation, Nat. Commun. 15 (1) (2024) 1587, https://doi.org/10.1038/s41467-024-45938-0.
[34] A. Sinclair, M.B. O'Kelly, T. Bai, H.C. Hung, P. Jain, S. Jiang, Self-healing Zwitterionic microgels as a versatile platform for malleable cell constructs and injectable therapies, Adv. Mater. 30 (39) (2018) e1803087, https://doi.org/10.1002/adma.201803087.
[35] J. Shi, P. Li, S. Kim, B. Tian, Implantable bioelectronic devices for photoelectrochemical and electrochemical modulation of cells and tissues, Nat Rev Bioeng 3 (6) (2025) 485–504, https://doi.org/10.1038/s44222-025-00285-7.
[36] D.F. Williams, Biocompatibility pathways and mechanisms for bioactive materials: the bioactivity zone, Bioact. Mater. 10 (2022) 306–322, https://doi.org/10.1016/j.bioactmat.2021.08.014.
[37] Y. Xia, X. Li, F. Huang, Y. Wu, J. Liu, J. Liu, Design and advances in antioxidant hydrogels for ROS-induced oxidative disease, Acta Biomater. 194 (2025) 80–97, https://doi.org/10.1016/j.actbio.2025.01.057.
[38] J. Su, C. Liu, A. Sun, J. Yan, F. Sang, Y. Xin, Y. Zhao, S. Wang, Q. Dang, Hemostatic and antimicrobial properties of chitosan-based wound healing dressings: a review, Int. J. Biol. Macromol. 306 (Pt 2) (2025) 141570, https://doi.org/10.1016/j.ijbiomac.2025.141570.
[39] D. Krasteva, Y. Ivanov, Z. Chengolova, T. Godjevargova, Antimicrobial potential, antioxidant activity, and phenolic content of grape seed extracts from four grape varieties, Microorganisms 11 (2) (2023), https://doi.org/10.3390/microorganisms11020395.
[40] O.A. Pena, P. Martin, Cellular and molecular mechanisms of skin wound healing, Nat. Rev. Mol. Cell Biol. 25 (8) (2024) 599–616, https://doi.org/10.1038/s41580-024-00715-1.
[41] C. Huang, L. Dong, B. Zhao, Y. Lu, S. Huang, Z. Yuan, G. Luo, Y. Xu, W. Qian, Anti-inflammatory hydrogel dressings and skin wound healing, Clin. Transl. Med. 12 (11) (2022) e1094, https://doi.org/10.1002/ctm2.1094.
[42] M. Keykhaee, F. Sorouri, M. Rahimifard, M. Baeeri, A. Forumadi, L. Firoozpour, M. Khoobi, Polysaccharide-based hydrogel enriched by epidermal growth factor peptide fragment for improving the wound healing process, Heliyon 9 (12) (2023) e22749, https://doi.org/10.1016/j.heliyon.2023.e22749.
[43] Z. Han, L. Dong, A. Li, Z. Li, L. Fu, Z. Zhang, X. Li, X. Li, Efficient angiogenesis-based wound healing through hydrogel dressing with extracellular vesicles release, Mater. Today Bio 16 (2022) 100427, https://doi.org/10.1016/j.mtbio.2022.100427.
[44] K. Ukaegbu, E. Allen, K.K.H. Svoboda, Reactive oxygen species and antioxidants in wound healing: mechanisms and therapeutic potential, Int. Wound J. 22 (5) (2025) e70330, https://doi.org/10.1111/iwj.70330.
[45] N.N. Mahmoud, K. Hamad, A. Al Shibitini, S. Juma, S. Sharifi, L. Gould, M. Mahmoudi, Investigating inflammatory markers in wound healing: understanding implications and identifying artifacts, ACS Pharmacol Transl Sci 7 (1) (2024) 18–27, https://doi.org/10.1021/acsptsci.3c00336.